

Halo Properties in Decaying Dark Matter Cosmology

衰變暗物質宇宙中的暗暈性質

CHEN, Jianxiong

陳健雄

A Thesis Submitted in Partial Fulfilment
of the Requirements for the Degree of
Doctor of Philosophy
in
Physics

The Chinese University of Hong Kong
March 2020

Thesis Assessment Committee

Professor LAW, Chi Kwong (Chair)

Professor CHU, Ming Chung (Thesis Supervisor)

Professor LI, Hua-Bai (Committee Member)

Professor NG, Kin Wang (External Examiner)

Abstract

We study the density profile of a dwarf halo in the decaying dark matter (DDM) cosmology, using a new algorithm that resolves halo density profiles down to the innermost 700 pc robustly with high efficiency. Following Schwarzschild’s orbit-based method, we have also developed a simplified model to calculate the DDM halo density profiles, which agree remarkably well with those from N-body simulations. Both zoom-in simulations and the simplified model reveal that dark matter decays lead to the flattening of central density and overall reduction of density in dwarf halos, and the underlying physics mechanisms are well illustrated by the simplified model. The slowly-rising scaled rotation curves of DDM dwarf halos agree with the observation of local dwarf galaxies. Our results suggest that the DDM holds great potential for resolving the small-scale problems faced by the cold dark matter (CDM) model.

摘要

我們研究衰變暗物質宇宙中矮星系的暗暈密度輪廓。採用新的N體模擬算法，我們以高的計算效率精確解析暗暈的密度輪廓至星系中心700 秒差距的範圍以內。應用施瓦西的軌道疊加方法，我們構建了一個簡化的數學模型來計算衰變暗物質模型下的暗暈密度輪廓。其計算結果與N體模擬取得了很好的吻合。細緻的N體模擬和簡化的數學模型都揭示出暗物質衰變導致暗暈密度輪廓在星系中心區域的平整化以及星系內暗物質密度的整體降低。簡化的數學模型清楚展示了背後的物理機制。緩慢上升的衰變暗物質暗暈自旋曲綫符合矮星系的天文觀測結果。我們的研究顯示衰變暗物質模型在解決冷暗物質模型的小尺度問題上有很好的潛力。

Acknowledgement

First of all, I would like to thank my supervisor Prof. Chu Ming Chung, who shows great patience and wisdom in the mentorship. Dr. Cheng Dalong, Dr. Liao Shihong and Dr. Zhang Jiajun lead me into the frontier of cosmology and N-body simulations, offer me numerical codes and answer my questions. To them I owe a debt of gratitude. I thank Dr. Volker Springel for offering me the P-GADGET3 code, which is vital for this work. I also benefit from the discussions with Mr. Liu Hantao, Mr. Lee Sze-Him, Mr. Leung Kiu-Ching and Mr. Lee Wai-Cheong. Sze-Him wrote a shell script for me to run DDM N-body simulations automatically.

I acknowledge the support of the CUHK Central High Performance Computing Cluster, on which the computation in this work has been performed. It is glad to thank Jim Law and Jason Chan for your technical supports in computing issues.

Specially, I would like to thank my spiritual family. You have always raised me up during the difficult times. Finally, thanks be to our Heavenly Father, who grants grace and reveals truth in our Lord Christ Jesus.

This work is dedicated to YHWH.

Contents

Abstract	i
Acknowledgement	iii
1 Introduction	1
1.1 Overview	1
1.2 Two-body relaxation and collisionless systems . .	7
1.3 N-body simulation method	13
1.4 A universal angular momentum profile for dark matter halos	16
2 DDM N-body algorithms	24
2.1 Overview of DDM N-body algorithms	24
2.2 An improved DDM algorithm	28
3 DDM dwarf halo density profiles	32
3.1 Cosmological zoom-in simulations	33
3.1.1 Numerical parameters calibration	37
3.1.2 High-resolution zoom-in halos	40
3.2 Mathematical modelling	42
3.2.1 Fundamental relations of decay	44
3.2.2 Schwarzschild modelling and orbit super- position	46
3.2.3 Two-step expansion	53
3.3 Results	58

3.4	Discussion	64
4	Conclusion	70
A	Angular momentum profile in stellar mass	73
B	Documentation for the code: DDMPLUGIN	75
B.1	Auxiliary daughter and permanent daughter . . .	75
B.2	Auxiliary-permanent transition	77
B.3	Decay of mother particles	79
C	Numerical tests	82
C.1	Transfer function	82
C.2	f_s	83
	Bibliography	85

List of Figures

1.1	Typical two-body encounter in N-body systems. \mathbf{v} is the velocity of an incoming subject particle. b is the impact parameter between the subject and field particles. Deflection $\delta\mathbf{v}$ is relatively small compared to \mathbf{v} due to the large separation between particles.	10
1.2	Illustration of the stacked specific angular momentum profile. Left panel: the specific angular momenta data from simulation halos in the mass bin $[4, 4\sqrt{2}] \times 10^{12} h^{-1} M_{\odot}$; Right panel: the universal profile $j_{\text{mod}}(r, \theta)$ with the three parameters j_s , r_s and θ_s fitted by the data shown in the left panel. This figure is taken from Liao et al. (2017) and is used with permission.	18

1.3	Comparison of the $j - M_\star$ relation for dark matter and HI gas. For each theoretical curve (dashed line), we fix the numerical values of r and θ and then calculate j_{mod} for different stellar mass M_\star . From top to bottom, the values for r are 1.0, 0.5, 0.25, and 0.1 respectively while θ is always $\pi/2$. See Appendix B for details of the evaluation procedure. Observation data for the average specific angular momentum of HI gas j_{gas} and stellar mass M_\star are taken from the following literatures: 16 blue points from Obreschkow & Glazebrook (2014), 14 black points from Butler et al. (2017), and 3 red points from Chowdhury & Chengalur (2017).	20
3.1	Large-scale environment of the selected dark matter halo, shown in a matter density map of a slice that contains the selected halo at $z = 0$. The depth of the slice is 0.1 times the parent simulation box size. The color encodes the local matter density in units of critical density ρ_{crit} . The two yellow circles are centred at the selected halo, with radii 1.0 Mpc/ h (solid) and 2.4 Mpc/ h (dotted). Within this sheet, no structures larger than galaxy-sized halo are found within 1.0 Mpc/ h range. All cluster-sized dark matter halos are outside 2.4 Mpc/ h . The data for this plot is taken from a level-12 CDM zoom-in simulation centred at the selected halo.	35

3.2	Effects of the numerical parameter n_f on the halo average density profile $\bar{\rho}(r)$. All profiles are measured at redshift 0 and all DDM zoom-in simulations use the same decay parameters: $V_k = 20.0$ km/s and $\tau^* = 3.0$ Gyr. Results are plotted towards the radii r_{rel} where the two-body relaxation time t_{rel} reaches the Hubble time H_0^{-1} . For both the left and right panels, the blue, green, red and black solid lines plot the results of the simulation using $n_f = 1, 3, 5$ and 10 , which is equivalent to that of the CCT15 algorithm, respectively. All these 4 zoom-in simulations are carried out at level 11. The left panel shows the density profiles of all level-11 runs and their relative differences to the profile from the CCT15 simulation. For $n_f = 1$, we also run a level-12 simulation. The right panel shows the relative differences between all level-11 density profiles and the level-12 density profile.	38
3.3	Illustration of orbits in the mathematical model. The red dashed lines are three elliptical orbits of daughter particles and the blue solid lines show three circular orbits of mother particles.	49
3.4	2D illustration of an elliptical orbit intersecting with a sphere. Point O is the center of the sphere in blue and the right focus of the ellipse in red. θ is the angle swept by a particle when it moves from point A to point C along the ellipse.	50
3.5	Upper panel: weighting factors for circular orbits. Lower panel: weighting factors for elliptical orbits with three different eccentricities: 0.1 (red), 0.5 (green), and 0.9 (blue).	52

3.6	Comparisons between the level-12 N-body simulation and the <i>SemiCore</i> calculation of the average density ratio $\bar{\rho}_{\text{ddm}}(r)/\bar{\rho}_{\text{cdm}}(r)$ between a DDM-CDM halo pair. In each subpanel, the solid red line shows the result of N-body simulations down to the innermost resolved radius r_{rel} . The light-blue shaded region outlines the prediction of the <i>SemiCore</i> model, where the upper and lower boundaries are given by the minimum and maximum expansion scenarios, respectively. The black dotted line shows the mass fraction of daughter particles inside each radius calculated from simulation data. The decay parameters used in each subpanel are implied by the DDM halo name (see Table 3.1 for details). For all N-body simulation curves, the statistical uncertainties from Poisson noises can be safely neglected for $r \geq r_{\text{rel}}$. The systematic uncertainty of our DDM algorithm introduces a $\sim 6\%$ uncertainty for $\bar{\rho}_{\text{ddm}}/\bar{\rho}_{\text{cdm}}$ at r_{rel} . The systematic uncertainties decrease as r increases and become unimportant (see Section 3.1.1 for details).	59
-----	---	----

3.7	Scaled inner rotation curves of the 9 level-12 DDM zoom-in dwarf halos. The rotation velocities $V_{\text{cir}}(r)$ are scaled by a characteristic velocity $V_{0.3}$ while the radii are scaled by $R_{0.3}$, where $V_{\text{cir}} = V_{0.3}$ and $d \ln V_{\text{cir}}/d \ln r = 0.3$. Simulation data are only shown for $r \geq r_{\text{rel}}$. The parent panel shows the results for the total matter field while the two sub-panels show the shapes for mother and daughter particles, respectively. Two theoretical curves are also plot for comparison, based on the NFW profile (black dotted line) and Burkert profile (black dot-dashed line).	62
3.8	Scaled rotation curves of the DDM halo V20T3 and 7 dwarf galaxies taken from THINGS [93]. The theoretical curves based on NFW and Burkert profiles are also plotted as black dotted line and dot-dashed line, respectively. The red soild line shows the curve of V20T3 for $r \geq r_{\text{rel}}$, where statistical uncertainties are negligible. The systematic uncertainty for $V_{\text{cir}}/V_{0.3}$ at r_{rel} is estimated to be about 3%. For larger radii, the systematic uncertainties become unimportant. We also have 2% uncertainty in the value of $R_{0.3}$, the effect of which on $V_{\text{cir}}/V_{0.3}$ can also be safely neglected. For the observational data, baryons have been subtracted. The light blue region is the prediction of the <i>SemiCore</i> model with the same set of decay parameters as V20T3. Error bars for the galaxy M81dwB are attached to show the typical uncertainty in observation.	65

3.9	Constrained DDM parameter space. The green-yellow region is ruled out by the Lyman- α forest data [39]. The DDM model in the light-blue region behaves like the CDM model in describing the cosmic structure formation. The gold region is outlined by Peter and Benson (2010) [41] and is interesting for small-scale problems of CDM. The blue and red points mark the 9 level-12 zoom-in dwarf halos in this work, with the blue and red color indicating cuspy and cored halo density profile respectively. For the blue point $V_k = 20.0$ km/s and $\tau^* = 6.93$ Gyr, the dynamics of Milky-Way satellite galaxies in the DDM model is explored in Wang et al. (2013). [39]. The brown strip is given by Abdelqader and Melia (2008) [40] where the deficit of dwarf galaxies in our local group can be accounted for in the DDM model. .	67
3.10	Relation between $R_{0.3}$ and $V_{0.3}$ for DDM zoom-in dwarf halos with the same half-life τ^* . The red circles, green diamonds and gray hexagons refer to halos with $\tau^* = 3.00, 6.93$, and 14.0 Gyr, respectively. There is 2% uncertainty in $R_{0.3}$ and 0.6% uncertainty in $V_{0.3}$. The best-fit power law curves for data points with $\tau^* = 3.00, 6.93$, and 14.0 Gyr are shown with red dashed, green dot-dashed and dotted line respectively. The best-fit power indexes are also shown near each line for reference.	68

C.1 Left panel: Effects of transfer function variation on dark matter halo average density profile $\bar{\rho}(r)$. Densities are normalized by the current critical density ρ_{crit} . The black solid lines are for the BBKS transfer function while red solid lines are for the Eisenstein-Hu transfer function, and the blue lines show the relative differences between them normalized by BBKS's results. The average density profile is not affected by the two-body relaxation for radii larger than $0.6 \text{ kpc}/h$. Right panel: Effects of the numerical parameter f_s on $\bar{\rho}(r)$. DDM simulations for this test all use $V_k = 20.0 \text{ km/s}$, $\tau^* = 3.0 \text{ Gyr}$ and $n_f = 1$. All profiles are measured at redshift 0 and plotted down to the inner-most resolved radii. The blue, red and black solid lines represent profiles for $f_s = 5, 10, 15$ respectively. The profiles with $f_s = 15$ serve as the baselines for comparison. 83

List of Tables

3.1	Halo properties of our simulation suite, including the name of each level-12 zoom-in simulation (column 1), recoil velocity of daughter particles (column 2), decay half-life (column 3), virial mass (column 4), virial radius (column 5), inner-most resolved radius (column 6), characteristic scale (column 7) and the corresponding characteristic velocity (column 8), concentration obtained from an NFW fitting (column 9), total particle number inside the virial radius (column 10). For the characteristic scale and velocity, see Section 3.3 for details	41
A.1	Model parameters for the specific angular momentum profile	74

Chapter 1

Introduction

1.1 Overview

Dark matter (DM) is a crucial ingredient of modern cosmology. It is needed to account for the anisotropy of the cosmic microwave background (CMB) [1, 2], large-scale structure formation and evolution [3], dynamics of galaxy clusters and groups [4], flattened rotation curves of late-type galaxies [5], and mismatch between mass centers revealed by gravitational lensing and X-ray emission respectively [6]. While the DM mass density is about 6 times higher than that of ordinary matter [7], its nature remains a mystery. Regardless of its composition, the microscopic properties of DM directly affect its cosmic mass dis-

tribution. Therefore, through a comparison between theoretical calculation and observation on DM distributions, properties of DM can be constrained.

Since 1970s, N-body simulation has become an indispensable theoretical tool for dealing with DM's nonlinear clustering. In 1980s, N-body simulations were used to rule out a neutrino-dominated Universe [8] and establish the canonical CDM model [9, 10, 11, 12]. With the improving resolution of N-body simulations, the inner structure of CDM halos were first resolved in 1990s [13, 14]. These high-resolution simulations revealed a central cusp in CDM halos, characterized by a power-law density profile $\rho(r) \propto r^{-\alpha}$ with $\alpha = 1$, independent of the halo mass. The cuspy density profile results in a steeply rising rotation curve as $V_{\text{cir}} \propto r^{1/2}$, which is incompatible with the observed solid-body rotation, $V_{\text{cir}} \propto r$, of dark matter-dominated dwarf and low surface brightness (LSB) galaxies [15, 16, 17]. The observed rotation curve suggests a flat density profile in the inner region of a halo. This tension is referred to as the *core-cusp* problem [18].

By the late 1990s, cosmological N-body simulations reached

the mass and force resolution that are needed to resolve subhalos as small as $10^8 M_\odot$ of a $10^{12} M_\odot$ galactic halo. Hundreds of subhalos down to the size of Draco and Ursa Minor system are revealed within the virial extent of a galactic halo in N-body simulations [19, 20]. At the same time, Milky Way galaxy and the nearby Andromeda galaxy each was found to have only tens of satellite galaxies [21]. The name of *missing-satellites* problem was thus coined to signify this significant difference between theoretical expectation and observational reality regarding satellite numbers [19]. Furthermore, the most massive subhalos of a N-body galactic halo are too massive to harbor the observed most luminous satellite galaxies of Milky Way. It is called the *too-big-to-fail* problem [22]. Together with other problems, the three well-known small-scale problems challenge the standard CDM model [23].

Within the CDM framework, the resolution of the small-scale problems relies on baryonic feedbacks. Take the *core-cusp* problem for example. The idea is that the energy released from starburst radiation or supernovae explosions is indirectly transferred to DM particles via frequent fluctuations of potential well

driven by repeated and fast gas outflows from the galactic centre [24, 25]. The extra energy gained by DM particles expands their orbits and converts an initial cuspy density profile into a cored one. The degree of conversion depends on the total energy released from feedbacks measured by stellar mass M_\star , the total baryonic matter M_b opposing the expansion, and the energy transfer efficiency. However, the last one is found to be very sensitive to the star formation gas density threshold n , a numerical parameter commonly adopted in sub-grid models of galaxy formation [26, 27]. Cosmological simulations with a large n report core formation in simulated dwarf galaxies [28, 29, 30] while the dark matter cusp remains in simulations using a smaller n [31]. Till now, a consensus has not been reached about whether baryonic processes can solve the *core-cusp* problem, and it continues to cast doubt on the CDM model.

Apart from the cored profile, many dwarf and LSB galaxies also have similar shape of rotation curves, implying a self-similar dark matter structure [32, 33]. This conformity is unlikely to be due to chaotic and dramatic baryonic processes [34, 35], but rather a clue to the nature of dark matter beyond CDM. In this

work we study a DDM model, which describes two-body decays of DM:

$$\psi^* \rightarrow \psi + l, \quad (1.1)$$

where ψ^* stands for the unstable mother DM particle, ψ is a massive stable daughter DM particle and l is a light and relativistic particle. The DM has therefore multiple components. The dynamics of the two-body decays in this model are fully controlled by two parameters: the decay rate Γ , or half-life $\tau^* = \ln 2/\Gamma$, of mother particles and ϵ the energy of l in unit of the mother particle's rest mass. The recoil velocity V_k of daughter particles in the center-of-mass frame of their mothers can be expressed as $V_k = \epsilon c$, where c is the speed of light.

There are diverse behaviours of the DDM model depending on the values of V_k and τ^* . For a very small τ^* such that almost all mother particles decay into daughter particles before any non-linear structures have formed, the DDM model is similar to the warm dark matter (WDM) model with a free-streaming length determined by the recoil velocity V_k [36, 37]. For a large V_k such that the decays convert a fair amount of energy from the matter component to the relativistic species, the expansion

history of the whole Universe will be altered [38]. For a broad range of τ^* while $V_k \lesssim 40$ km/s, the 1D Lyman- α forest power spectrum predicted by the DDM model is shown to be consistent with observation data [39], implying that the model behaves like CDM at large scale. Inside a parameter region outlined by $10.0 \lesssim V_k \lesssim 40.0$ km/s (or equivalently $3.0 \times 10^{-5} \lesssim \epsilon \lesssim 1.3 \times 10^{-4}$) and $0.1 \lesssim \tau^* \lesssim 14$ Gyr, decays significantly heat up DM inside dwarf-sized halos, and are relevant for the small-scale problems of CDM [40, 41, 42]. In light of this, we revisit the *core-cusp* problem and study the density profiles of dwarf halos in the DDM model using high-resolution cosmological N-body simulations, which are absent from previous studies.

In Section 1.2, we introduce an important physical process in a N-body system: two-body relaxation. The concept of collisionless systems is also clarified. Then we introduce the N-body simulation method in Section 1.3. A universal angular momentum distribution pattern for CDM dark matter halos are presented in Section 1.4, as an example of the application of N-body simulation in the theoretical study of dark matter halos.

1.2 Two-body relaxation and collisionless systems

Consider a dynamical system composing of N gravitationally-interacting particles. The acceleration of one of the particles can be written as the summation of two components:

$$g = g_{ngb} + g_{glb}. \quad (1.2)$$

The component g_{ngb} arises from the perturbations exerted by its nearest-neighbour particles. The other component g_{glb} signifies the contributions from the rest of the system. As the effects of gravity extend to infinity, the term g_{glb} does not vanish. On the contrary, the acceleration of a particle is largely determined by the large scale contribution g_{glb} [43]. As a function of time, g_{glb} is very smooth since the noisy part of g is accounted for by g_{ngb} . In general, for a self-gravitating system with $N \gtrsim 1000$, its constituents accelerate smoothly and do not undergo violent scatterings, which are usually found in a system governed by a short-range force [43, 44].

Although small relative to g_{glb} , accumulated deflections induced

by g_{ngb} will gradually randomize particles' motion till the memory of their initial velocities is lost. This process is called the two-body relaxation. The small noisy term g_{ngb} plays an important role in the secular evolution of a N-body system, for example, the mass segregation phenomenon observed in globular clusters [44]. To estimate the timescale over which the two-body relaxation is important, we consider the following simple model as shown in Figure 1.1: a subject particle approaches a fixed field particle with velocity \mathbf{v} along a trajectory with an impact parameter b . Suppose the field particle only perturbs the subject particle slightly, then a straight-line can be applied to approximate the path of the subject particle. The velocity deviation $\delta\mathbf{v}(b)$ caused by the encounter is given by the following integration:

$$\delta\mathbf{v}(b) = \int_{-\infty}^{\infty} \frac{\mathbf{F}dt}{m}, \quad (1.3)$$

where \mathbf{F} is the gravitational force between the subject and field particles while m is their mass. Taking the symmetry of the model into consideration, one can find the magnitude of the velocity deviation

$$\delta v(b) = \frac{2Gm}{bv}, \quad (1.4)$$

where G is the Newtonian gravitational constant. The velocity deviation is perpendicular to the subject particle's path and points to the side where the field particle sits. From Equation (1.4) it is clear that the approximation is valid when b is larger than $2Gm/v^2$. We label this critical impact parameter as b_c . For a bound system of size R , the typical velocity of particles can be estimated as the circular velocity at the edge of the system:

$$v = \sqrt{\frac{GNm}{R}}. \quad (1.5)$$

Then the typical b_c of the system is around R/N . On the other hand, d_c , the mean separation between particles, is roughly $R/\sqrt[3]{N}$. For a large N , b_c is much smaller than d_c . Hence for our interest, Equation (1.4) is well established.

Since the direction of each perturbation is random and particles experience similar scatterings, the mean velocity of the system is not affected by the neighbouring two-body interactions. What has changed is the velocity dispersion σ^2 . After each particle is randomly perturbed by a neighbouring particle with impact parameter b , σ^2 of the system is increased by an

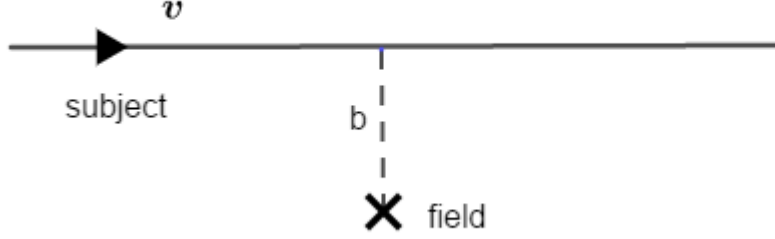


Figure 1.1: Typical two-body encounter in N-body systems. \mathbf{v} is the velocity of an incoming subject particle. b is the impact parameter between the subject and field particles. Deflection $\delta\mathbf{v}$ is relatively small compared to \mathbf{v} due to the large separation between particles.

amount of $\delta v^2(b)$. Consider the timescale t_{cross} during which each particle has at least crossed the system once. For every crossing, each particle will encounter $N(b)$ neighbouring particles with an impact parameter of b , on average. The value of $N(b)$ can be estimated as follows:

$$N(b) = \frac{N}{\pi R^3} 2\pi b R db = \frac{2N}{R^2} b db, \quad (1.6)$$

where $N/\pi R^3$ gives the mean particle number density of the system. The increment of σ^2 after t_{cross} is just adding up the contribution from different impact parameter:

$$\Delta\sigma^2(t_{cross}) = \int_{b_c}^{d_s} N(b) \delta v^2(b). \quad (1.7)$$

We choose the upper limit of the integration to be d_s as $\Delta\sigma^2$ is mainly induced by neighbouring particles. The integration gives

$$\Delta\sigma^2(t_{cross}) = 8N \left(\frac{2Gm}{Rv} \right)^2 \ln \Lambda. \quad (1.8)$$

The factor $\ln \Lambda$ is called the Coulomb logarithm and has the following form:

$$\ln \Lambda = \ln \left(\frac{d_s}{b_c} \right) \sim \ln N. \quad (1.9)$$

Roughly the time dependence of $\Delta\sigma^2$ can be expressed as

$$\Delta\sigma^2(t) = \Delta\sigma^2(t_{cross}) \frac{t}{t_{cross}}. \quad (1.10)$$

The timescale t_{relax} is defined such that the change of the system's velocity dispersion reaches the same order of magnitude of v^2 . Then from Equation (1.10) one can derive the expression for t_{relax} as

$$t_{relax} = \frac{v^2}{\Delta\sigma^2(t_{cross})} t_{cross}. \quad (1.11)$$

Using Equation (1.5) to eliminate v from Equation (1.11) and noticing that $\ln \Lambda \sim \ln N$, we relate t_{relax} to the crossing time

t_{cross} in a simple form:

$$t_{relax} \simeq \frac{0.1N}{\ln N} t_{cross}. \quad (1.12)$$

The crossing time t_{cross} can be estimated as R/v where R is the size of the system and v is particles' typical velocity. For N-body systems with lifetime larger than t_{relax} , the effect of cumulative kicks between individual particles have grown enough to influence the system's dynamics. This kind of systems is called collisional. To integrate a collisional system, the acceleration given by encounters with neighbouring particles cannot be neglected from Equation (1.2). A typical globular cluster has 10^5 stars and a crossing time of 0.5 Myr. Then its typical relaxation time is about 0.4 Gyr. Since globular clusters generally have an age of 10 Gyr, the two-body relaxation must be taken carefully in the dynamical study of these celestial systems.

On the other hand, systems with lifetime smaller than t_{relax} are called collisionless. Galaxies and dark matter are its well-known examples. For collisionless systems, the two-body scatterings are unimportant, hence can be neglected. Then the motion of an individual particle is governed by the potential of an

underlying smooth density distribution, rather than a discrete density distribution as it seems. Therefore the complexity of the problem is largely reduced. For this thesis, we focus on the study of collisionless systems.

1.3 N-body simulation method

Modern cosmology thrives from several simple ideas: an extremely hot, dense and uniform initial condition, an expanding spacetime described by general relativity with a cosmological constant Λ , and exotic invisible weakly-interacting matter dominating the matter component. Simple or crazy as it looks, the model has great prediction power and is generally recognized as the standard model for the observable universe: the Λ CDM model, where CDM refers to the exotic invisible cold dark matter. In a universe filled with cold dark matter, initial overdensities are amplified via gravity and form gravitational-bound structures named dark matter halos. Structure formation then proceeds in a bottom-up way: larger dark matter halos are formed through the merging and accretion of smaller halos. Smaller halos could survive and orbit within larger halos.

Galaxy formation occurs in the central region of dark matter halos. Hence the large-scale distribution of galaxies is a biased tracer for the underlying distribution of dark matter. Theoretical calculation of dark matter distribution and populating galaxies inside them bridges theory and observation, which boosts the development of cosmology over the past half century.

As the number of elementary dark matter particles is huge, they can be safely approximated as a collisionless fluid. Their phase-space distribution function $f(\mathbf{x}, \mathbf{v}, t)$ obeys the collisionless Boltzmann equation:

$$\frac{df}{dt} = \frac{\partial f}{\partial t} + \mathbf{v} \frac{\partial f}{\partial \mathbf{x}} - \frac{\partial \Phi}{\partial \mathbf{x}} \frac{\partial f}{\partial \mathbf{v}} = 0, \quad (1.13)$$

where $\Phi(\mathbf{x}, t)$ is the gravitational potential, which couples to the density field $\rho(\mathbf{x}, t)$ via the Poisson equation:

$$\nabla^2 \Phi(\mathbf{x}, t) = 4\pi G \rho(\mathbf{x}, t). \quad (1.14)$$

The coupled partial differential equations (1.13) and (1.14) are difficult to be solved analytically, especially when the density field $\rho(\mathbf{x})$ becomes more and more inhomogeneous. The N-body

simulation method is in essence the method of characteristics for solving partial differential equations. The phase-space distribution $f(\mathbf{x}, \mathbf{v}, t)$ are sampled by N simulation particles with their masses being the sampling weights. Each simulation particle traces a characteristic trajectory and the solution of the partial differential equations can be estimated from the distribution of these N bodies. The N-body method reduces the partial differential equations (1.13) and (1.14) to $2N$ ordinary differential equations:

$$\frac{d\mathbf{x}_i}{dt} = \mathbf{v}_i, \quad (1.15)$$

and

$$\frac{d\mathbf{v}_i}{dt} = \sum_{j \neq i} \mathbf{g}_{ij}, \quad (1.16)$$

where \mathbf{g}_{ij} is the gravitational acceleration of the simulation particle i induced by simulation particle j . Due to the long-range nature of gravity, the summation in Equation (1.16) needs to go through all other simulation particles. Hence the heart of a N-body simulation is to evaluate the gravitational force for every simulation particle. To do this, the most straightforward way is the direct summation illustrated by Equation (1.16), which

is commonly adopted in early N-body simulations [45, 46, 47]. As the algorithm complexity of direct summation scales as N^2 , it becomes unrealistic for large N system ($N \gtrsim 1000$). Fast algorithms have been developed for large N simulations, including the particle-mesh algorithm [48] and the tree algorithm [49]. They both have $N \ln N$ complexity. Now the N-body simulation algorithm with Newtonian gravity has matured. Results of different algorithms achieved good convergence. A comprehensive review on this subject can be found in [50].

1.4 A universal angular momentum profile for dark matter halos

Like density, angular momenta inside dark matter halos are known to follow certain distribution pattern [51, 52, 53]. By stacking halos with similar masses from the Bolshoi simulation [54], Liao et al. found that the resulting internal distribution of specific angular momenta¹ has a universal profile [55]. It can be parameterized by a simple and cylindrically symmetric

form:

$$j_{\text{mod}}(r, \theta) = j_s \frac{(r/r_s)^2}{(1 + r/r_s)^4} \sin^2(\theta/\theta_s), \quad (1.17)$$

where r is the dimensionless radial distance to the center of a halo in unit of the halo's virial radius R_{vir} , while j_s , r_s and θ_s are three fitting parameters. The total angular momentum of the halo points to the direction specified by $\theta = 0$. Figure 1.2 illustrates this universal profile. It reveals the feature that low specific angular momentum matter locate in a conical volume around the halo's rotation axis. This is quite different from a rigid body rotation. On the other hand, matter with high specific angular momenta are distributed within a donut-like region near the outermost edge of the halo's equatorial plane.

The parameter j_s is closely related to halo's mass M_{vir} as

$$\frac{j_s}{h^{-1} \text{Mpc} \text{ kms}^{-1}} = (3.63 \pm 0.16) \left(\frac{M_{\text{vir}}}{10^{10} h^{-1} M_{\odot}} \right)^{0.660 \pm 0.006}, \quad (1.18)$$

which reflects the angular momentum–mass relation $j \propto M_{\text{vir}}^{2/3}$ of virialized dark matter halos [56]. The radial scale parameter

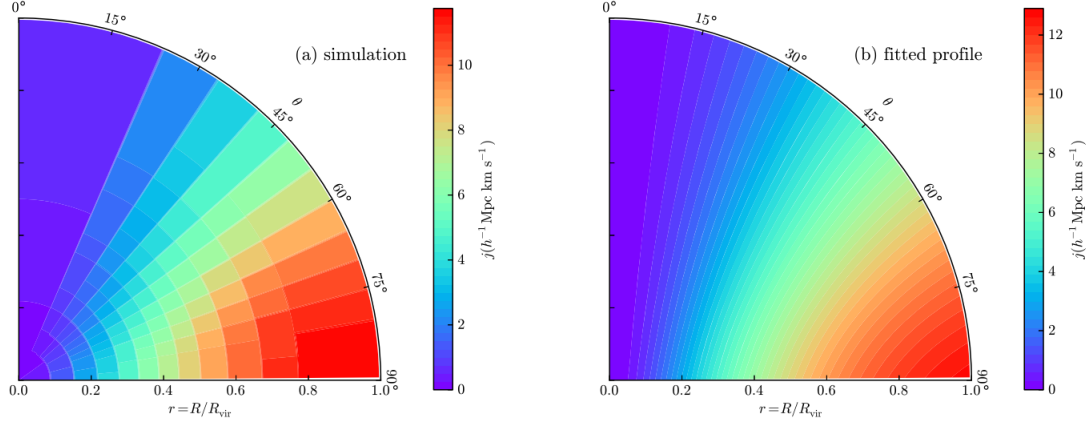


Figure 1.2: Illustration of the stacked specific angular momentum profile. Left panel: the specific angular momenta data from simulation halos in the mass bin $[4, 4\sqrt{2}] \times 10^{12} h^{-1} M_{\odot}$; Right panel: the universal profile $j_{\text{mod}}(r, \theta)$ with the three parameters j_s , r_s and θ_s fitted by the data shown in the left panel. This figure is taken from Liao et al. (2017) and is used with permission.

r_s has a weak dependence on M_{vir} and is parameterized as

$$r_s = (0.95 \pm 0.04) \left(\frac{M_{\text{vir}}}{10^{10} h^{-1} M_{\odot}} \right)^{0.040 \pm 0.006}. \quad (1.19)$$

Another scale parameter θ_s does not show clear dependence on M_{vir} and is approximated as a constant:

$$\theta_s = 1.096. \quad (1.20)$$

Hence the stacked specific angular momentum profile $j_{\text{mod}}(r, \theta)$ can be easily calculated once the halo mass M_{vir} is given. In practice, by using the stellar mass-halo mass relation [57, 58, 59],

M_{vir} can be inferred observationally from M_\star , the mass of the galaxy's stellar component. Therefore, the specific angular momentum profile of a dark matter halo, on average, can be measured indirectly by weighing its stars.

In the classical theory of disk galaxy formation under the Λ CDM cosmology, initially the gas and dark matter share the same specific angular momentum distribution as they feel the same gravitational torque exerted by the surrounding large-scale environment [60, 61, 62, 63]. The universal profile (1.17) suggests that the specific angular momentum at any spatial position within a halo scales approximately with the halo mass as

$$j_{\text{mod}}(r, \theta) \propto M_{vir}^{2/3}. \quad (1.21)$$

Then before the gas is cooled, the average specific angular momentum of the gas locating at volume V ,

$$j_{\text{gas}} \approx \frac{\int_V j_{\text{mod}}(r, \theta) \rho_{\text{gas}}(r) dV}{\int_V \rho_{\text{gas}}(r) dV}, \quad (1.22)$$

is expected to follow a similar mass scaling, $j_{\text{gas}} \propto M_{vir}^{2/3}$. In

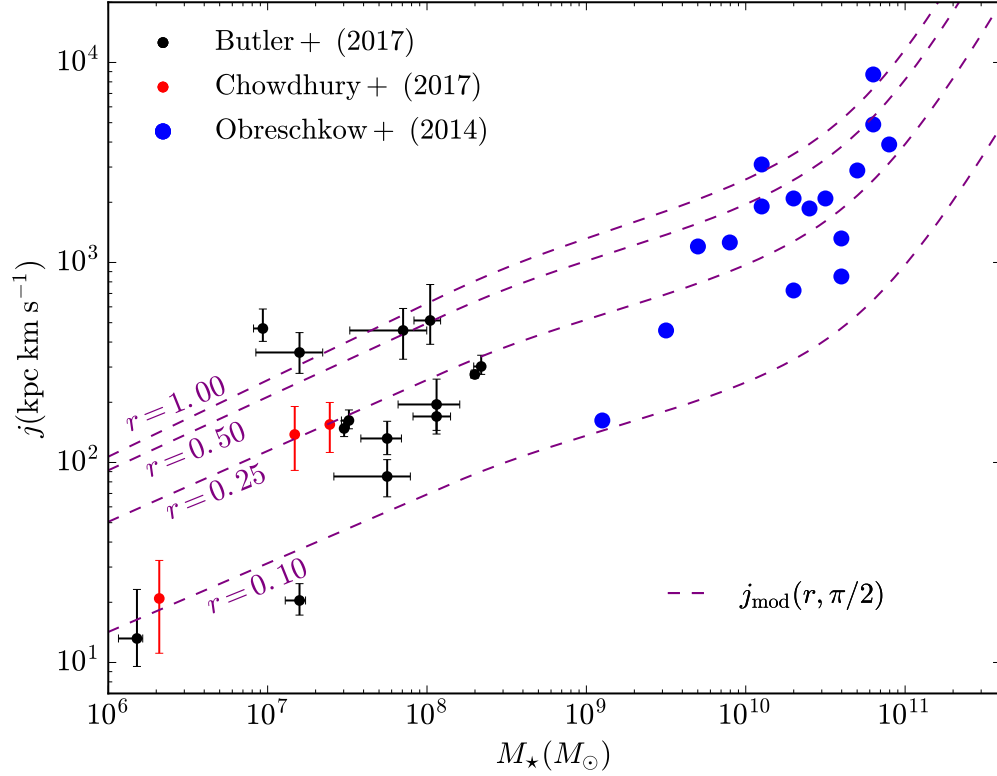


Figure 1.3: Comparison of the $j - M_{\star}$ relation for dark matter and HI gas. For each theoretical curve (dashed line), we fix the numerical values of r and θ and then calculate j_{mod} for different stellar mass M_{\star} . From top to bottom, the values for r are 1.0, 0.5, 0.25, and 0.1 respectively while θ is always $\pi/2$. See Appendix B for details of the evaluation procedure. Observation data for the average specific angular momentum of HI gas j_{gas} and stellar mass M_{\star} are taken from the following literatures: 16 blue points from Obreschkow & Glazebrook (2014), 14 black points from Butler et al. (2017), and 3 red points from Chowdhury & Chengalur (2017).

Figure 1.3, we compare the observed $j_{gas} - M_*$ relations of HI gas [64, 65, 66] and the $j_{mod}(r, \theta) - M_*$ scaling at different positions. We find that indeed the observed $j_{gas} - M_*$ relation has the same universal shape as $j_{mod}(r, \theta) - M_*$ relation (at any r and θ). This implies that although the detailed processes are fairly complicated (e.g., cooling, feedbacks, torques, etc.), the HI gas condenses out from different parts of a halo in a way that does not depend on halo masses.

The universal angular momentum profile $j_{mod}(r, \theta)$ is useful in studying the angular momenta of virialized halos. Given a density profile $\rho(r)$, one can calculate many angular momentum-related quantities, such as the total angular momentum J , the spin parameter λ [53, 61] and the angular momentum distribution $M(j)/M_{vir}$, where $M(j)$ is the total mass with specific angular momentum smaller than j [53]. As mentioned earlier in this section, $M(j)/M_{vir}$ serves as a good approximation to the distribution of j_{gas} at a galaxy's very early stage. By comparing $M(j)/M_{vir}$ with the current distribution of j_{gas} in low mass disk galaxies [67], people found that a significant fraction of gas with

low angular momentum is missing from the observed dwarf disk galaxies. In a disk galaxy, gases having low angular momenta are located near its central region. To account for this discrepancy, galactic winds from supernova explosions are thought to be responsible for removing low angular momentum gas from a galaxy's center [68]. Later, this mechanism was confirmed by hydrodynamic simulations [28, 69].

For theoretical interest of an equilibrium collisionless system, the universal angular momentum profile $j_{\text{mod}}(r, \theta)$ is also helpful. It is an important complement to the universal density profile $\rho(r)$. With the knowledge of $j_{\text{mod}}(r, \theta)$, the degeneracy of the distribution function $f(\boldsymbol{x}, \boldsymbol{v})$ can be largely reduced. Then a clearer phase space structure of the equilibrium collisionless system can be obtained. The understanding of this universal angular momentum profile $j_{\text{mod}}(r, \theta)$ can deepen our understanding of the dynamics of a collisionless system. The search of its origin is a challenging theoretical work and the answer remains unknown. The situation highlights the importance of N-body simulation in the theoretical study of collisionless systems. It is interesting

to study how dark matter and cosmological models will affect $j_{\text{mod}}(r, \theta)$. These works will shed more light on the origin of this universal angular momentum profile.

□ **End of chapter.**

¹Specific angular momentum here refers to the angular momentum per unit mass which is parallel to the total angular momentum \mathbf{J} of the whole halo. The components which are perpendicular to \mathbf{J} are not considered.

Chapter 2

DDM N-body algorithms

We discuss N-body algorithms for the DDM model in this chapter. In Section 2.1 we review previous DDM algorithms, summarizing their advantages as well as shortcomings. In Section 2.2, we describe our improved DDM algorithm in detail.

2.1 Overview of DDM N-body algorithms

In the DDM model, the light particle l does not take part in the structure formation directly, and is ignored in the following discussion. The Boltzmann equations for the mother particle ψ^* and daughter particle ψ are

$$\frac{df_{\psi^*}}{dt} = -\frac{\ln 2}{\tau^*} f_{\psi^*}, \quad (2.1)$$

and

$$\frac{df_\psi}{dt} = \frac{\ln 2}{4\pi\tau^*V_k^2} \int f_{\psi^*}(\mathbf{r}, \mathbf{v}', t) \delta(|\mathbf{v} - \mathbf{v}'| - V_k) d^3\mathbf{v}', \quad (2.2)$$

respectively, where f_{ψ^*} and f_ψ are the corresponding phase-space mass densities. The DDM matter density evolution can be simulated by using the N-body method once the collision terms in Equations (2.1) and (2.2) are properly handled. The first DDM N-body simulation was presented in Peter et al. (2010, hereafter PMK10) [70], where the DDM model (1.1) was realized on simulation particle basis. In PMK10, each mother simulation particle has a decay probability. Once chosen for decay, the mother simulation particle is flagged to be a daughter simulation particle and receives a random velocity kick at the same time. This Monte-Carlo sampling of decays is carried out at each simulation timestep. Therefore, the global decay rate $\ln 2/\tau^*$ is sampled continually and precisely for the whole system, while the local decay rate fluctuates around the global value with an amplitude depending on the local number density of mother simulation particles. As time goes on, the total number of mother simulation particles drops and the matter density field becomes

more and more nonlinear. It can be seen that the decay sampling precision of PMK10 is not uniform in both space and time domains. It is also an intrinsic challenge for the PMK10 algorithm to resolve the central structures of DM halos due to the limited number of mother simulation particles there.

To achieve a uniform decay sampling in both space and time domains, Cheng et al. (2015, hereafter CCT15) [71] proposed a DDM algorithm based on a discretization of the Boltzmann equations (2.1) and (2.2). In CCT15, decays are only sampled at several simulation timings, when each mother simulation particle is split partly to generate a new daughter simulation particle which is kicked randomly at its birth. At other simulation times, all simulation particles are evolved according to the collisionless Boltzmann equation:

$$\frac{df_{\psi^*(\psi)}}{dt} = 0. \quad (2.3)$$

The number of mother particles is kept unchanged, and the mass-splitting procedure is the same for all mother simulation particles. Therefore, the decays can be sampled uniformly both in space and time domains. Two numerical parameters are introduced in this algorithm: f_s , the number of mass-splittings

throughout a simulation, and N_s , the number of daughter simulation particles produced per mother simulation particle at each mass-splitting.

Consider a simulation following the CCT15 algorithm with f_s splittings. Initially it has N mother simulation particles. As each mass-splitting procedure generates $N_s N$ daughter simulation particles, the total number of daughter simulation particles will increase to $f_s N_s N$ by the end of the simulation. For typical values that achieve satisfactory numerical convergence, such as $f_s = 10$ and $N_s = 1$, the final number of daughter simulation particles is larger than that of mother simulation particles by an order of magnitude. Generally the number of simulation particles serves as a measure of the precision of an N-body simulation. However for daughter simulation particles, this measure does not apply to the both CCT15 and PMK10 algorithms, because the phase space distribution of daughter particles is inferred from N discrete mother simulation particles, not from an underlying continuous distribution function. The sampling resolution of daughter simulation particles is limited by that of the mother simulation particles, which is set in the initial condition.

Hence, increasing the number of daughter simulation particles contributes little to improving the simulation’s resolution. On the other hand, the large demand for computing resources of the CCT15 algorithm hinders its practical usage in large cosmological simulations. Therefore improvement of the CCT15 algorithm is needed for our purpose of running high resolution zoom-in simulations.

2.2 An improved DDM algorithm

We follow the framework outlined in CCT15 but improve on it. In our algorithm, the mother simulation particles decay and give birth to daughter simulation particles only at a limited number of decay instances, called breakpoints. The breakpoints are ordered on the time axis in a way that in each phase, the time interval between two adjacent breakpoints, the same number of mother simulation particles decay into daughter simulation particles. When a breakpoint is reached, each mother simulation particle is splitted into a less-massive mother simulation particle and a daughter simulation particle according to the decayed fraction. The newly generated daughter simulation parti-

cles are called auxiliary daughters. The mass-splitting procedure increases the total number of simulation particles by N . To save memory as well as to speed up the whole simulation, we only track the motion of these N auxiliary daughters for each phase. When the simulation arrives at the next breakpoint, the auxiliary daughters born at the last breakpoint will undergo a random selection process such that only a fraction of them η survive and are renamed as permanent daughters. The remaining auxiliary daughter particles are eliminated so that the memory occupied by them is released. All permanent daughters will be traced to the end of the simulation. Therefore there are two states of the daughter simulation particles in our scheme: auxiliary and permanent.

The auxiliary daughters help to conserve the local matter mass when a decay occurs, a basic conservation observed in both CCT15 and PMK10. After diffusing into the environment, these auxiliary daughters are replaced by permanent daughters, which have a smaller population, hence heavier. The transition from the auxiliary state to permanent state decreases the resolution of daughter particles. Though numerical side-effects

can be introduced from the resolution degradation, it is controllable by tuning the survival fraction η . Suppose there are N mother simulation particles initially and they go through f_s breakpoints. When the simulation is finished, there are $n_f N$ permanent daughters in total, with $n_f = \eta f_s$. Setting $\eta = 1$ brings our algorithm back to CCT15. We implement this algorithm in an individual module named DDMPLUGIN, see Appendix B for details. It is designed to be compatible with other N-body codes such that the physics associated with dark matter decay is self-contained. This is achieved as follows: during each phase, the whole system is evolved by an N-body CDM code. When a breakpoint is reached, the system's final state is output to the DDMPLUGIN module, which implement the physical effects of dark matter decays. Hence an updated system state is generated. The DDMPLUGIN module then outputs this new state to be the initial condition for next phase's evolution, which is again tracked by the N-body CDM code. Therefore our DDM simulation can be easily implemented in any N-body code, an advantage rooted in the CCT15 algorithm.

□ **End of chapter.**

Chapter 3

DDM dwarf halo density profiles

In this chapter, we present the main results of this thesis. Section 3.1 introduces our simulation methods and overviews our high-resolution zoom-in dwarf halo suite. Section 3.2 details the construction of a simplified model for density profile calculation in the DDM model. The results of N-body simulations and the simplified model are presented in Section 3.3, and their observational implications are discussed in Section 3.4.

3.1 Cosmological zoom-in simulations

To study the density profiles of dark matter halos in the DDM cosmology, we run cosmological zoom-in simulations [72] using the DDMPLUGIN module with the N-body code P-GADGET3, a descendant of the public TreePM code GADGET2 [73]. In all simulations, a flat geometry with a cosmological constant is assumed for the background cosmology, where the cosmological parameters are taken from the final results of Planck TT,TE, EE+lowE measurements: $\Omega_m = 0.3166$, $\Omega_\Lambda = 0.6834$, $h = 0.6727$, $n_s = 0.9649$ and $\sigma_8 = 0.8120$ [74]. Initial conditions are generated by using the code MUSIC [75] with the BBKS transfer function [76]. The uncertainties induced by the choice of transfer functions are characterized in Appendix C.1. The effect turns out to be negligible. Dark matter halos are identified by the halo finder AHF [77, 78], with Bryan and Norman’s fitting formula [79] for overdensity Δ_c calculation. For our adopted cosmology, dark matter halos at redshift $z = 0$ are defined by the virial radius R_{vir} within which the mean overdensity is about 103.4 times the critical density ρ_{crit} . Using the position of the halo centre, the virial radius, and the best

Navarro-Frenk-White (NFW) profile fit provided by AHF, we collect all particles bound to the target halo and use our own code to measure its radial mass distribution $\bar{\rho}(r)$, the average matter density inside radius r :

$$\bar{\rho}(r) = \frac{3M(r)}{4\pi r^3}, \quad (3.1)$$

where $M(r)$ is the enclosed mass. The two-body relaxation time t_{rel} is estimated for certain radii using the method documented in [43]. Only those radii with t_{rel} larger than the Hubble time H_0^{-1} are considered to be reliably resolved [80].

To select a candidate halo for zoom-in simulations, we run a full-box CDM cosmological simulation starting from redshift 99. It uses 256^3 simulation particles inside a periodic cubic box with a width of 6.73 Mpc/ h , corresponding to a physical length of 10.0 Mpc at $z = 0$. Each CDM simulation particle has a mass of $1.59 \times 10^6 M_\odot/h$, which is the coarse resolution of the full-box simulation. We select dark matter halos at redshift 0 by two criteria: small Lagrangian volume and being isolated from larger structures. The selected dark matter halo has a

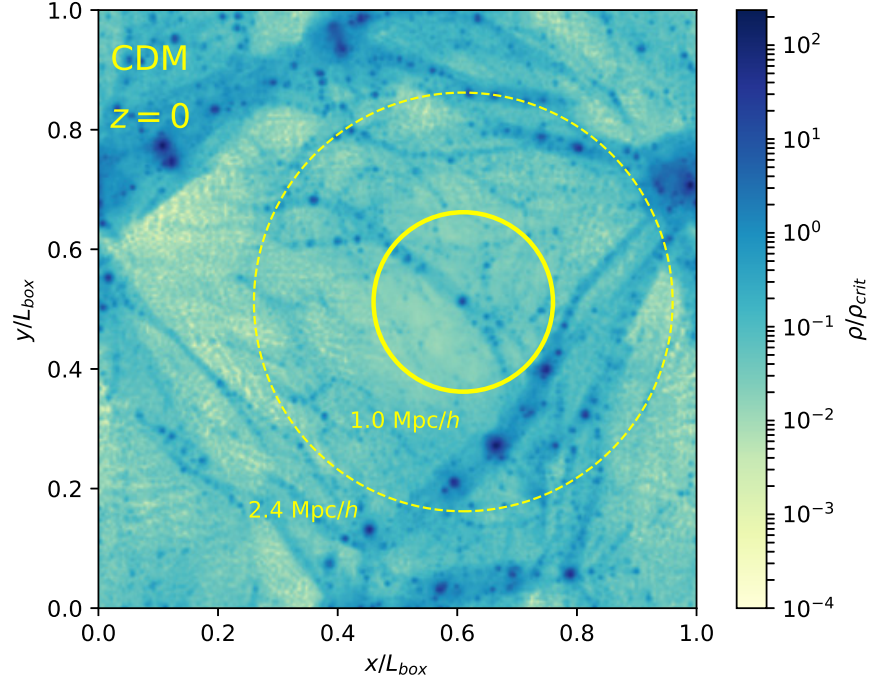


Figure 3.1: Large-scale environment of the selected dark matter halo, shown in a matter density map of a slice that contains the selected halo at $z = 0$. The depth of the slice is 0.1 times the parent simulation box size. The color encodes the local matter density in units of critical density ρ_{crit} . The two yellow circles are centred at the selected halo, with radii 1.0 Mpc/ h (solid) and 2.4 Mpc/ h (dotted). Within this sheet, no structures larger than galaxy-sized halo are found within 1.0 Mpc/ h range. All cluster-sized dark matter halos are outside 2.4 Mpc/ h . The data for this plot is taken from a level-12 CDM zoom-in simulation centred at the selected halo.

virial mass $M_{\text{vir}} = 5.17 \times 10^9 M_{\odot}/h$ and an NFW concentration $c_{\text{vir}} = 21.6$, closely following the theoretically motivated $c - M$ relation of Diemer and Joyce [81]. Its large-scale environment is illustrated in Figure 3.1, showing that the selected halo is far away from surrounding larger structures.

For zoom-in simulations centred at the selected halo, the initial density fluctuations inside its Lagrangian volume are sampled by high-resolution particles while its large-scale environment is represented by coarse resolution particles. A buffer volume is created between the above two regions to avoid large resolution gradient. We label the resolution level of a zoom-in simulation by an integer l . A level- l zoom-in simulation has a mass resolution equivalent to that of a full-box N-body simulation using $(2^l)^3$ CDM particles in its initial condition. We adopt the empirical formula recommended by Power et al. [82] to calculate the gravitational softening lengths for high-resolution CDM zoom-in simulation particles. As for DDM zoom-in simulations, the decays of mother simulation particles are only switched on inside the high-resolution volume. It is reasonable since we do

not consider decay parameters that result in significant deviations from the CDM large-scale matter distribution. Gravitational softening lengths for high-resolution DDM particles are set to be the same as those of CDM zoom-in particles which have the same resolution level. This reflects our consideration that the resolution of a DDM simulation is constrained by its initial condition. We also require that zoom-in halos are free of contamination by lower resolution particles within their virial radii for a clean analysis. In the following section, we carry out convergence test and calibrate f_s and n_f of our DDM algorithm for dark matter halo density profile study.

3.1.1 Numerical parameters calibration

The parameter f_s controls the decay sampling frequency, and a larger value of it leads to a finer sampling of the decay history. In CCT15, the total number of daughter particles is linearly proportional to f_s . Hence it cannot be arbitrarily large, otherwise the computational work load will be huge. However this constraint on f_s is released in our algorithm as the total number

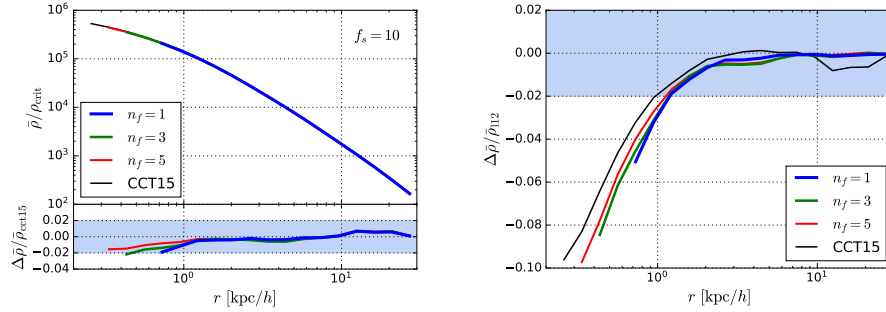


Figure 3.2: Effects of the numerical parameter n_f on the halo average density profile $\bar{\rho}(r)$. All profiles are measured at redshift 0 and all DDM zoom-in simulations use the same decay parameters: $V_k = 20.0$ km/s and $\tau^* = 3.0$ Gyr. Results are plotted towards the radii r_{rel} where the two-body relaxation time t_{rel} reaches the Hubble time H_0^{-1} . For both the left and right panels, the blue, green, red and black solid lines plot the results of the simulation using $n_f = 1, 3, 5$ and 10 , which is equivalent to that of the CCT15 algorithm, respectively. All these 4 zoom-in simulations are carried out at level 11. The left panel shows the density profiles of all level-11 runs and their relative differences to the profile from the CCT15 simulation. For $n_f = 1$, we also run a level-12 simulation. The right panel shows the relative differences between all level-11 density profiles and the level-12 density profile.

of daughter particles is solely determined by $n_f N$. For DDM zoom-in simulations used in this study, we set $f_s = 10$ by default. It proves to be large enough for acceptable numerical convergences (see Appendix C.2 for details) .

In our algorithm, n_f controls the total number of simulation particles. To test its effects on the halo average density profile, we tried three values: $n_f = 1, 3$, and 5 . A simulation using the CCT15 algorithm (equivalent to $n_f = f_s$) is also carried out for

comparison. All simulations are run in level-11 resolution using the same decay parameters $V_k = 20.0$ km/s and $\tau^* = 3.0$ Gyr. The density profiles at $z = 0$ are measured down to the inner-most resolved radii and are shown in the left panel of Figure 3.2. The density profiles with different values of n_f all converge to CCT15’s density profile within 2% at all resolved radii. This implies that the radial mass distribution $\bar{\rho}(r)$ is insensitive to the value of n_f when $n_f \geq 1$. We further run a level-12 simulation using the same decay parameters for $n_f = 1$. In the right panel of Figure 3.2, we compare all level-11 profiles with the level-12 one. For $r \lesssim 1.0$ kpc, all level-11 profiles are systematically lower than the level-12 profile. The differences continue to grow when r approaches to the halo centre. A large n_f does help to narrow the differences down, however the cost is also huge: the gain in precision is only about 3% by increasing n_f from 1 to 10 (the CCT15 algorithm). As a larger value of n_f brings forth a larger number of simulation particles, the two-body relaxation converged radius r_{rel} decreases as the value of n_f increases. However, for $n_f > 1$, r_{rel} cannot be taken as the inner-most resolved radii anymore, because the deviation from

the level-12 profile at r_{rel} also grows with the n_f and reaches 10% level for $n_f \geq 5$. Hence for the level-11 runs, increasing the value of n_f cannot push inward the inner-most resolved radius reliably. On the contrary, the innermost resolved limit set by the r_{rel} of the $n_f = 1$ run is worthy: the density profile of the level-11 resolution converges to that of the level-12 resolution within 5% for all radii larger than 0.8 kpc/ h . Then we can safely use $n_f = 1$ without worrying about possible degradation of resolution and take r_{rel} as the inner-most resolved radius. For our highest resolution zoom-in simulations, the level-12 runs, we use $n_f = 1$ and $f_s = 10$. The results are presented in the next section.

3.1.2 High-resolution zoom-in halos

Our level-12 simulation suite comprises 10 cosmological zoom-in simulations: 1 CDM and 9 DDM realizations. All 10 simulations use the same initial condition at redshift 99. The high-resolution volume in the initial condition is a cuboid with three edge-lengths being 0.09, 0.09 and 0.15 Mpc/ h , centering at its

Table 3.1: Halo properties of our simulation suite, including the name of each level-12 zoom-in simulation (column 1), recoil velocity of daughter particles (column 2), decay half-life (column 3), virial mass (column 4), virial radius (column 5), inner-most resolved radius (column 6), characteristic scale (column 7) and the corresponding characteristic velocity (column 8), concentration obtained from an NFW fitting (column 9), total particle number inside the virial radius (column 10). For the characteristic scale and velocity, see Section 3.3 for details

Name	V_k [km/s]	τ^* [Gyr]	M_{vir} [$10^9 M_\odot/h$]	R_{vir} [kpc/h]	r_{rel} [kpc/h]	$R_{0.3}$ [kpc/h]	$V_{0.3}$ [km/s]	c_{nfw}	N_p $\times 10^7$
CDM	—	—	5.17	35.0	0.254	0.407	27.7	21.6	1.33
V20T3	20.0	3.00	4.22	32.7	0.291	0.904	26.0	15.0	2.35
V20T7	20.0	6.93	4.41	33.2	0.224	0.805	27.4	17.3	2.36
V20T14	20.0	14.0	4.70	33.9	0.200	0.684	28.7	19.3	2.41
V30T3	30.0	3.00	2.89	28.8	0.366	1.72	20.1	6.99	1.93
V30T7	30.0	6.93	3.32	30.2	0.254	1.23	23.3	11.4	1.91
V30T14	30.0	14.0	4.05	32.3	0.215	0.810	26.4	16.8	2.08
V40T3	40.0	3.00	0.350	14.3	0.470	3.58	10.0	4.64	0.377
V40T7	40.0	6.93	1.79	24.6	0.278	1.69	18.1	9.93	1.19
V40T14	40.0	14.0	3.26	30.0	0.234	1.00	23.7	13.5	1.67

parent simulation box. The mass of each high-resolution particle is $3.89 \times 10^2 M_\odot/h$. The gravitational softening length of high-resolution CDM particles is set to be 3.36×10^{-2} kpc/h, frozen to a physical length about 50 pc after $z = 10$. All DDM realizations follow the same softening length assignment scheme such that the force resolution of our simulation suite is uniform. All our zoom-in halos are free of contamination by low-resolution particles within their virial radii. The 9 DDM realizations differ

from each other in the combination of V_k and τ^* . We have used 3 values of τ^* : 3.0, 6.93 and 14.0 Gyr, with corresponding decayed fractions 0.959, 0.748 and 0.495, respectively, at redshift 0. For each τ^* , we use 3 different values of V_k : 20.0, 30.0 and 40.0 km/s. These 9 realizations constitute a rough sampling of the interesting region in the $\tau^* - V_k$ parameter space. Halo expansion has been observed in the 9 DDM zoom-in halos as they generally have smaller virial masses but lower concentrations compared to the corresponding CDM halo. The virial masses, virial radii and other global properties of all zoom-in halos are summarized in Table 3.1. We study the physics accounting for the DDM halo expansion in the next section.

3.2 Mathematical modelling

Due to its unparallel accuracy, cosmological N-body simulation is indispensable for studying the density profiles of dark matter halos. However, simulation alone does not help us to gain insight into the problem of interest. The primary physics mechanisms that shape the results are hidden within the complex simulation machinery. On the other hand, high accuracy is achieved only

through the high usage of computational resources. Hence it is unrealistic for running large-scale simulations to survey the 2-dimensional parameter space of our DDM model. In order to get a simple understanding on the DDM density profiles and to study the density profile's dependence on V_k and τ^* , we construct a mathematical model to calculate the DDM density profile.

The halo expansion in the DDM model is driven by two primary physical processes. The first one is the decay itself. On average, the kinetic energy of newly born daughter particles are greater than those of their mothers. This extra kinetic energy drives the orbits of daughters outwards, hence expanding the whole halo. We call this the Step-1 expansion. A consequence of this expansion is the weakening of the gravitational potential, triggering the Step-2 expansion: the bulk particles' orbits expand outwards to rebalance the weakened gravity with the inertial force seen in the orbits' rotating frames. Cen [83] considers a special case of the two-step expansion: $V_k \gg v_e$ and $\tau > t_{\text{dyn}}$, where v_e and t_{dyn} are the halo's typical escape velocity and dy-

namical time, respectively. The large V_k unbinds all daughter particles during the Step-1 expansion while the slow decay simplifies the Step-2 evolution to an adiabatic expansion. Starting from an NFW density profile, the resulting density profile turns out to remain an NFW shape, but with a smaller concentration and a lower normalization density (see also the relevant discussion in Peter [84]). Sánchez-Salcedo [85] considers the situation where most of daughter particles are bound to the halo ($V_k < v_e$) and the halo expands adiabatically ($\tau > t_{\text{dyn}}$). Through simple semi-analytic calculations, he argued that the cored profile is a natural result of the two-step expansion. In this section, we propose a general formalism to implement the two-step expansion for $\tau > t_{\text{dyn}}$.

3.2.1 Fundamental relations of decay

The model assumes that a dark matter halo forms at a high redshift when only a small fraction of mother particles have decayed. Initially the halo is CDM-like with an NFW density profile. Then decays proceed and the density profile evolves.

The decay of a mother particle is a random process and does not have a preferential direction. On average, each new-born daughter particle acquires an additional amount of kinetic energy from the mass deficit of its mother particle:

$$\begin{aligned}
E_{k,\text{dau}} &= \frac{1}{2}m_{\text{dau}}\langle \mathbf{v}_{\text{dau}}^2 \rangle \\
&= \frac{1}{2}m_{\text{dau}}\langle (\mathbf{v}_{\text{mom}} + V_k \mathbf{n})^2 \rangle \\
&= \frac{1}{2}m_{\text{dau}}v_{\text{mom}}^2 + \frac{1}{2}m_{\text{dau}}V_k^2 + m_{\text{dau}}V_kv_{\text{mom}}\langle \cos \theta \rangle \quad (3.2) \\
&= \frac{1}{2}m_{\text{mom}}v_{\text{mom}}^2 \frac{m_{\text{dau}}}{m_{\text{mom}}} + \frac{1}{2}m_{\text{dau}}V_k^2 \\
&= \frac{m_{\text{dau}}}{m_{\text{mom}}}E_{k,\text{mom}} + \frac{1}{2}m_{\text{dau}}V_k^2,
\end{aligned}$$

where m_{dau} and m_{mom} are the masses of daughter particles and mother particles, respectively, V_k is the recoil velocity of the daughter particle in its mother's center of mass frame, E_k stands for the kinetic energy, $\langle \dots \rangle$ indicates the mean of the expression inside, \mathbf{n} is a unit vector with random direction, and θ is the angle between \mathbf{n} and \mathbf{v}_{mom} . Since the mass difference between m_{dau} and m_{mom} is very small, $(m_{\text{mom}} - m_{\text{dau}})/m_{\text{mom}} = V_k/c$, where c is the speed of light, hereafter we approximate the ratio

m_{dau}/m_{mom} as 1 for simplicity:

$$E_{k,dau} = E_{k,mom} + \frac{1}{2}m_{dau}V_k^2. \quad (3.3)$$

Similarly, one can find that the mean angular momentum of a daughter particle is the same as that of its mother:

$$\mathbf{L}_{dau} = \mathbf{L}_{mom}, \quad (3.4)$$

where \mathbf{L} stands for the orbital angular momentum of a particle. Equation (3.3) and Equation (3.4) are referred to as the fundamental relations of decay. They are the cornerstone on which our mathematical model is built.

3.2.2 Schwarzschild modelling and orbit superposition

As both mother and daughter particles are collisionless, in principle one can use the distribution function of particles to describe their dynamics. However, due to its time-dependence, it is hard to model the distribution function even though the whole system remains spherically symmetric [43]. Then we turn to the orbit-based method, which was first proposed by Martin

Schwarzschild [86]. We refer readers to the literature [87] for a short overview. In Schwarzschild’s model, a collisionless system is represented by a large library of particle orbits. Physical quantities, such as mass distribution, are then derived through constructing superpositions of these orbits. We adopt this method to build our mathematical model.

Given a gravitational potential $\Phi(r)$, an individual particle’s orbit is a function of the particle’s total energy E and angular momentum \mathbf{L} . Generally the joint distribution of E and \mathbf{L} gives the ensemble of particle orbits. To keep the model simple, we assume all mother particles take circular orbits around the halo center and the normal vector to each orbital plane points to a random direction. Although unrealistic [88, 89], the circular-orbit assumption is a good starting point. First of all, regarding the halo density profile, the physics that makes the DDM model different from the CDM model is maintained by this assumption. The simple dynamics of circular motion simplifies the calculation and model building. As a result, the physics of interest is easier to be demonstrated. Secondly, nearly circular orbits are more common than nearly radial orbits inside a halo [90, 84], and

so the circular orbit is not a bad representation of the whole library of orbits. Finally, in the study of halo's response to the condensation of gas near a galaxy's center, it has been shown that calculations based on circular-orbit assumption have a satisfactory match with simulation results [91]. For a model with a primary focus on physics rather than accuracy, it is enough to assume circular orbits for mother particles. As for daughter particles, we approximate their orbits as ellipses since on average the energy of a daughter particle is higher than its mother's while their angular momenta are the same. Note that the halo centre sits at one of the foci of these ellipses. Hence in our model, there are two types of orbits: circular orbits of mother particles and elliptical orbits of daughter particles.

Now we consider the enclosed mass profile $M(R)$ as a superposition of orbits. Mathematically, all orbits in the library form a set. We name it as *Olib*. For each element x in *Olib*, a weighting factor $g_x(R)$ is assigned such that $M(R)$ is the summation

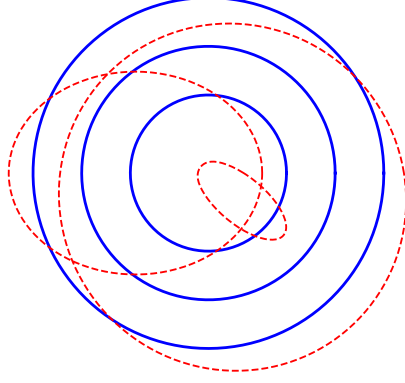


Figure 3.3: Illustration of orbits in the mathematical model. The red dashed lines are three elliptical orbits of daughter particles and the blue solid lines show three circular orbits of mother particles.

of all $g_x(R)$ over the set $Olib$:

$$M(R) = \sum_{x \in Olib} m_x g_x(R), \quad (3.5)$$

where m_x is the mass of the particle moving in the orbit x . The weighting factor $g_x(R)$ can be constructed as the fraction of time the particle spends inside the sphere $r = R$:

$$g_x(R) = \Delta t_x(R) / T_x, \quad (3.6)$$

where $\Delta t_x(R)$ is the duration that a particle travels inside the

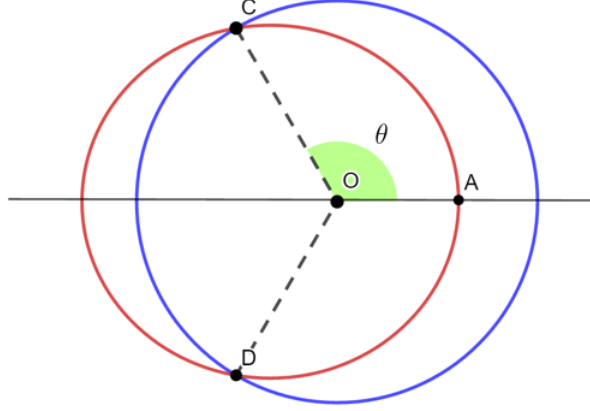


Figure 3.4: 2D illustration of an elliptical orbit intersecting with a sphere. Point O is the center of the sphere in blue and the right focus of the ellipse in red. θ is the angle swept by a particle when it moves from point A to point C along the ellipse.

sphere $r = R$ within an orbital period T_x . For circular orbits, their weighting factors $g_{\text{cir}}(r/R)$ are step functions since a circle with radius r is either totally inside or totally outside the sphere R :

$$g_{\text{cir}}(r/R) = \begin{cases} 0 & \text{if } r/R > 1, \\ 1 & \text{if } r/R \leq 1. \end{cases} \quad (3.7)$$

Similarly, for an elliptical orbit with semi-major axis a and eccentricity e , if its perihelion r_{\min} is larger than R , then its weighting factor $g_{\text{ell}}(a/R, e)$ vanishes. If its aphelion r_{\max} is smaller than R , then $g_{\text{ell}}(a/R, e)$ takes the value of 1. Apart from the above two totality cases, elliptical orbits can also in-

intersect with the sphere $r = R$, as shown in Figure (3.4). Since the angular momentum is an integral of the motion, the weighting factor of the intersecting case can also be easily derived:

$$g_{\text{ell}}(a/R, e) = \frac{\int_0^\theta \frac{d\phi}{(1+e \cos \phi)^2}}{\int_0^\pi \frac{d\phi}{(1+e \cos \phi)^2}}, \quad (3.8)$$

where the integral limit θ is given by

$$\theta = \arccos \left[\frac{a(1 - e^2) - R}{eR} \right]. \quad (3.9)$$

To conclude, the weighting factor of elliptical orbits takes the following form:

$$g_{\text{ell}}(a/R, e) = \begin{cases} 0 & \text{if } R \leq r_{\min}(a, e), \\ \frac{\int_0^\theta \frac{d\phi}{(1+e \cos \phi)^2}}{\int_0^\pi \frac{d\phi}{(1+e \cos \phi)^2}} & \text{if } r_{\min}(a, e) < R < r_{\max}(a, e), \\ 1 & \text{if } R \geq r_{\max}(a, e). \end{cases} \quad (3.10)$$

θ is determined by Equation (3.9). $r_{\min}(a, e) = a(1 - e)$ and $r_{\max}(a, e) = a(1 + e)$. The shape of the function $g_{\text{ell}}(a/R, e)$ is determined by the eccentricity e , as shown in Figure (3.5). When e approaches to zero, the function $g_{\text{ell}}(a/R, e)$ approaches

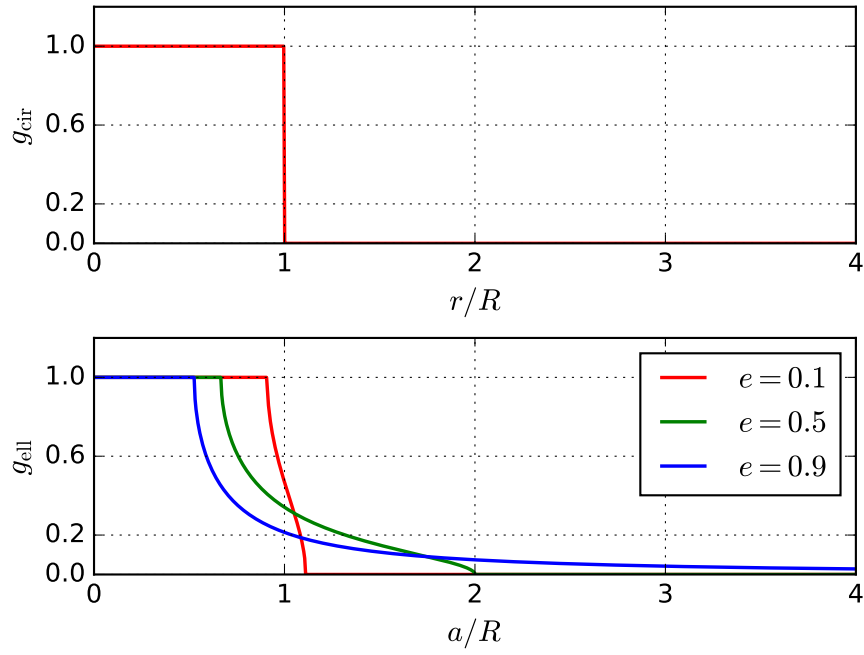


Figure 3.5: Upper panel: weighting factors for circular orbits. Lower panel: weighting factors for elliptical orbits with three different eccentricities: 0.1 (red), 0.5 (green), and 0.9 (blue).

to a step function, which is the form of $g_{\text{cir}}(r/R)$ of circular orbits. When e is close to unity, the function $g_{\text{ell}}(a/R, e)$ becomes much broader and has a nonvanishing value for orbits with semi-major axis a ranging from 0 to $R/(1 - e)$. As a is proportional to the total energy E of an elliptical orbit, the broadness of g_{ell} implies that high energy orbits mix up with low energy orbits inside the sphere of radius R . This orbital mixing feature does not occur among circular orbits as they never cross each other.

3.2.3 Two-step expansion

Consider the Step-1 expansion during a small time interval Δt such that the gravitational potential $\Phi(r)$ remains static. The decay randomly acts on the circular orbits of mother particles and then transform them into ellipses of daughter particles. Consider a pair of them: a circular orbit with radius r_0 before decay and the corresponding elliptical orbit with semi-major axis a and eccentricity e after decay. According to Equation (3.4), they share the same specific angular momentum l_0 , thus the

same effective potential:

$$V_{\text{eff}} = \frac{l_0^2}{2r^2} + \Phi(r). \quad (3.11)$$

The value of l_0 can be obtained by considering the circular motion at radius r_0 , where V_{eff} reaches its minimum. As for the elliptical orbit, its perihelion and aphelion are the two roots of the following equation from Equation (3.3):

$$V_{\text{eff}}(r) - V_{\text{eff},\min} - \frac{1}{2}V_k^2 = 0, \quad (3.12)$$

where

$$V_{\text{eff},\min} = V_{\text{eff}}(r_0). \quad (3.13)$$

By solving Equation (3.12), one can find the perihelion r_{\min} and the aphelion r_{\max} of the daughter particle's orbit. They both depend on the radius r_0 of its mother particle's orbit. From r_{\min} and r_{\max} the semi-major axis a and the eccentricity e are obtained:

$$a = \frac{r_{\max} + r_{\min}}{2}, \quad (3.14)$$

and

$$e = \frac{x - 1}{x + 1}, \quad (3.15)$$

where $x = r_{\max}/r_{\min}$. For a V_k such that Equation (3.12) has two distinct roots, each decay transfers a circular orbit with radius r_0 ,

$$R_{\text{cir}}(\theta) = r_0, \quad (3.16)$$

into an elliptical orbit,

$$R_{\text{ell}}(\theta) = \frac{a(1 - e^2)}{1 + e \cos \theta}, \quad (3.17)$$

where a and e are functions of r_0 and V_k . For large V_k such that Equation (3.12) has only one root, each decay removes one circular orbit out of the library of orbits.

After Δt , the mass increment of daughter particles inside the sphere $r = R$ can be calculated by considering the contributions from the daughter particles which are born during this time interval:

$$\Delta M_{\text{dau}}(R, \Delta t, t_i) = \Delta f \int_0^\infty 4\pi r^2 \rho_{\text{mom}}(r, t_i) g_{\text{ell}}[a(r, V_k)/R, e(r, V_k), t_i] dr, \quad (3.18)$$

where Δf is the fraction of mother particles decayed during Δt :

$$\Delta f = \log(2)\Delta t/\tau^*. \quad (3.19)$$

$\rho_{\text{mom}}(r, t_i)$ is the density profile of mother particles at time t_i . The mass profile of mother particles declines uniformly by a factor of Δf :

$$\Delta M_{\text{mom}}(R, \Delta t, t_i) = -\Delta f M_{\text{mom}}(R, t_i). \quad (3.20)$$

Then after the Step-1 expansion, the total mass profile $M(R)$ changes by an amount of

$$\Delta M(R, \Delta t, t_i) = \Delta M_{\text{dau}}(R, \Delta t, t_i) - \Delta f M_{\text{mom}}(R, t_i). \quad (3.21)$$

We proceed to consider the Step-2 expansion in the time interval $(t_i, t_i + \Delta t)$. For mother particles, the adiabatic expansion for circular orbits reads:

$$RM(R, t_i) = R_f(t_{i+1})[M(R, t_i) + \Delta M(R, \Delta t, t_i)], \quad (3.22)$$

from which the radius at $t_{i+1} = t_i + \Delta t$, $R_f(t_{i+1})$, can be derived. Initially the total mass of mother particles inside R is

$M_{\text{mom}}(R, t_i)$. After Δt , the total mass of mother particles inside $R_f(t_{i+1})$ is $(1 - \Delta f)M_{\text{mom}}(R, t_i)$. Therefore the mass profile $M_{\text{mom}}(R, t)$ evolves a bit. For daughter particles, there is no simple formula to treat their adiabatic expansion as they have elliptical orbits. To deal with this issue, we propose two scenarios: minimum expansion and maximum expansion. For the former, we do not apply the Step-2 expansion to daughter particles, which means that after Δt , the mass profile of daughter particles changes from $M_{\text{dau}}(R, t_i)$ to $M_{\text{dau}}(R, t_i) + \Delta M_{\text{dau}}(R, \Delta t, t_i)$. For the latter, we treat daughter particles' expansion in the same manner as mother particles'. The difference between the two scenarios serves an uncertainty estimation of our modelling.

Through the two-step expansion we have evolved the whole system from t_i to t_{i+1} . We loop the procedures listed above and evolve the whole system from the initial time t_0 to the final time t_f .

3.3 Results

The simplified semi-analytic model presented in Section 3.2 is implemented with a numerical code called *SemiCore*. Convergence is achieved as the total number of timesteps increases. Starting from the best-fit NFW profile of the level-12 CDM halo ($M_{\text{vir}} = 5.17 \times 10^9 M_{\odot}/h$ and $c_{\text{vir}} = 21.6$), we run *SemiCore* with the combinations of V_k and τ^* listed in Table 3.1, with the initial and final times being the same as those of cosmological N-body simulations. For each pair of V_k and τ^* , two parallel *SemiCore* runs are carried out: one with the minimum expansion scenario and the other with the maximum expansion scenario. In Figure 3.6, we show the present ($z = 0$) average density profile ratios, $\bar{\rho}_{\text{ddm}}(r)/\bar{\rho}_{\text{cdm}}(r)$, between the DDM-CDM halo pairs which evolve from the same primeval local overdensity field. We compare the results of the *SemiCore* model with those from the level-12 N-body simulations. For the *SemiCore* model, $\bar{\rho}_{\text{cdm}}(r)$ is calculated from the input NFW profile.

The simulation data reveals that dark matter decays reduce the mass profile throughout the dwarf halos. The global reduction amplitude increases as V_k increases or as τ^* decreases. For

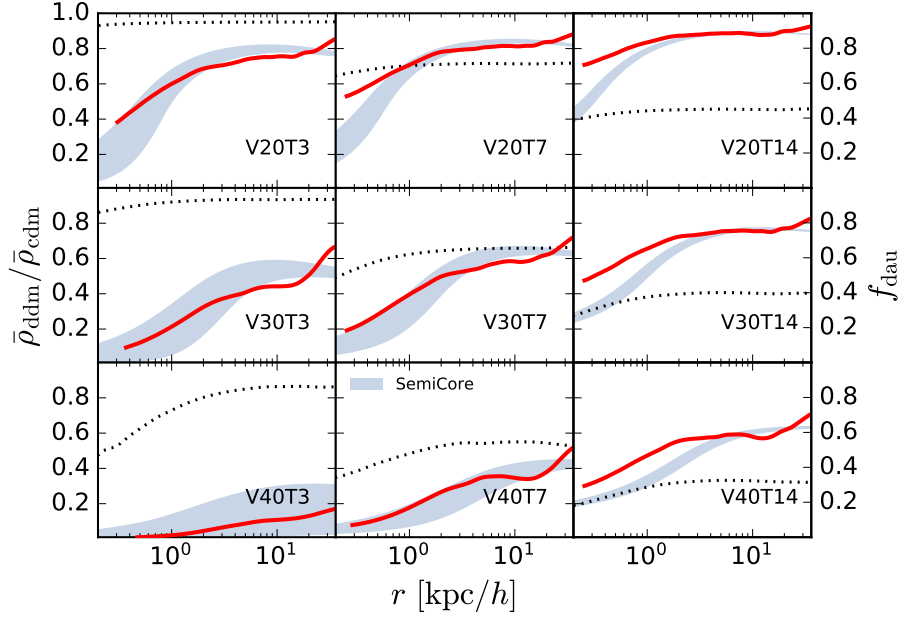


Figure 3.6: Comparisons between the level-12 N-body simulation and the *SemiCore* calculation of the average density ratio $\bar{\rho}_{\text{ddm}}(r)/\bar{\rho}_{\text{cdm}}(r)$ between a DDM-CDM halo pair. In each subpanel, the solid red line shows the result of N-body simulations down to the innermost resolved radius r_{rel} . The light-blue shaded region outlines the prediction of the *SemiCore* model, where the upper and lower boundaries are given by the minimum and maximum expansion scenarios, respectively. The black dotted line shows the mass fraction of daughter particles inside each radius calculated from simulation data. The decay parameters used in each subpanel are implied by the DDM halo name (see Table 3.1 for details). For all N-body simulation curves, the statistical uncertainties from Poisson noises can be safely neglected for $r \geq r_{\text{rel}}$. The systematic uncertainty of our DDM algorithm introduces a $\sim 6\%$ uncertainty for $\bar{\rho}_{\text{ddm}}/\bar{\rho}_{\text{cdm}}$ at r_{rel} . The systematic uncertainties decrease as r increases and become unimportant (see Section 3.1.1 for details).

a given pair of decay parameters, the difference between DDM and CDM halos becomes more pronounced as r approaches to the halo center. These trends are well reproduced by the *SemiCore* model. Furthermore, the average density ratios $\bar{\rho}_{\text{ddm}}/\bar{\rho}_{\text{cdm}}$ predicted by *SemiCore* agree with those from sophisticated N-body simulations to better than 40%, for all resolved radii and for all combinations of V_k and τ^* considered in this study. The triumph of *SemiCore* confirms the two-step expansion scenario for explaining the halo expansion induced by dark matter decays.

The agreements are remarkably good for smaller τ^* s, where daughter particles dominate the halo's dynamical evolution. For the three runs with $\tau^* = 14.0$ Gyr and the run with $V_k = 20.0$ km/s and $\tau^* = 6.93$ Gyr, *SemiCore* systematically overpredicts the mass reduction in the inner region ($r \lesssim 0.1R_{\text{vir}}$). This overestimation can be traced to the simplified assumption of circular orbits for all mother particles. In the *SemiCore* model, many mother particles are removed completely from the enclosed mass after the adiabatic expansion, because of the sharp transition of the weighting factor g_{cir} , from 1 to 0. In reality, most of the

simulation particles take up elliptical orbits [88, 89], and so the weighting factors for their orbits should be g_{ell} (see Figure 3.5), which is non-zero even after adiabatic expansion of the orbits. This implies over-suppression of the density of mother particles, and the effect is particularly pronounced near a halo’s center, where the mother particles are perturbed more by decays. The same effect was observed in modelling adiabatic contraction of dark matter by circular orbits, which leads to an enhancement of the central density relative to the results of high resolution simulations [89]. In the outer region ($r \gtrsim 0.8R_{\text{vir}}$), N-body simulations show that the ratios $\bar{\rho}_{\text{ddm}}/\bar{\rho}_{\text{cdm}}$ continue to grow while the *SemiCore* model predicts a flattened or slightly declining shape. This may be due partly to the fact that the decay of a mother particle in an elliptical orbit produces an even more elliptical daughter orbit, compared to that from a circular orbit. So the daughter particles should reach larger r on average. There may also be mass accretion from the environment, which is absent in the *SemiCore* model.

In Figure 3.6, the average density ratios from N-body simulations display a common shape: rising inner and outer re-

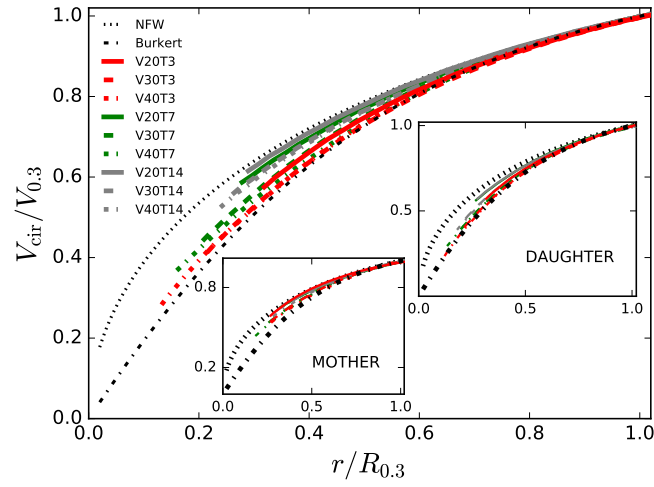


Figure 3.7: Scaled inner rotation curves of the 9 level-12 DDM zoom-in dwarf halos. The rotation velocities $V_{\text{cir}}(r)$ are scaled by a characteristic velocity $V_{0.3}$ while the radii are scaled by $R_{0.3}$, where $V_{\text{cir}} = V_{0.3}$ and $d \ln V_{\text{cir}}/d \ln r = 0.3$. Simulation data are only shown for $r \geq r_{\text{rel}}$. The parent panel shows the results for the total matter field while the two subpanels show the shapes for mother and daughter particles, respectively. Two theoretical curves are also plot for comparison, based on the NFW profile (black dotted line) and Burkert profile (black dot-dashed line).

gions connected by an extended plateau. A positive slope of the $\bar{\rho}_{\text{ddm}}/\bar{\rho}_{\text{cdm}}$ curve implies the flattening of DDM density profile compared to that of its CDM counterpart. For a clear verification, we calculate the rotation curve $V_{\text{cir}}(r)$, scaled by $V_{0.3}$, the circular velocity at radius $R_{0.3}$ where $d \ln V_{\text{cir}}/d \ln r = 0.3$ [92]. In Figure 3.7, we plot the scaled rotation curves for all level-12 DDM halos, and their values of $R_{0.3}$ and $V_{0.3}$ are listed in Table 3.1. The scaled rotation curves based on the cuspy NFW profile and cored Burkert profile [34] are also plotted together for comparison. The DDM curves spread between the two theoretical curves in two groups. One is made up of 4 DDM halos: V20T14, V30T14, V40T14 and V20T7. Their scaled rotation curves are closer to the NFW curve than the Burkert one. The remaining 5 halos form the second group which features a significant deviation from the NFW curve and is much closer to the Burkert curve. We further plot the scaled rotation curves for the mother and daughter components in Figure 3.7. The scaled rotation curves for daughter particles are clearly lower than the NFW curve. Surprisingly, 7 out of 9 daughter curves cling to the Burkert curve with small scatters among them. The two

outliers are V20T7 and V20T14. Their combination of small V_k and large τ^* leads to a weaker expansion compared to other halos. As for the mother particles, halos V20T3, V20T7, V20T14, and V30T14 are slightly below the NFW curve and follow its trend closely. The other 5 halos are intermediate between NFW and Burkert, signaling stronger DDM effect captured in N-body simulations.

3.4 Discussion

The flattening of the central density of dwarf halos is needed to resolve the *core-cusp* problem of CDM. In Figure 3.8, we compare DDM's results with CDM's and observational data. Halo V20T3 is a representative case for the flattened DDM rotation curves, resolved down to $r = 0.3R_{0.3}$. We also show the results of the *SemiCore* as a reference. The observed scaled rotation curves of 7 dwarf galaxies' dark matter component from *The HI Nearby Galaxy Survey* (THINGS) [93] are consistent with those of both the DDM simulation V20T3 and the simplified model *SemiCore* within considerable scatters, while they clearly deviate from the NFW curve systematically for $r \lesssim 0.4R_{0.3}$. Al-

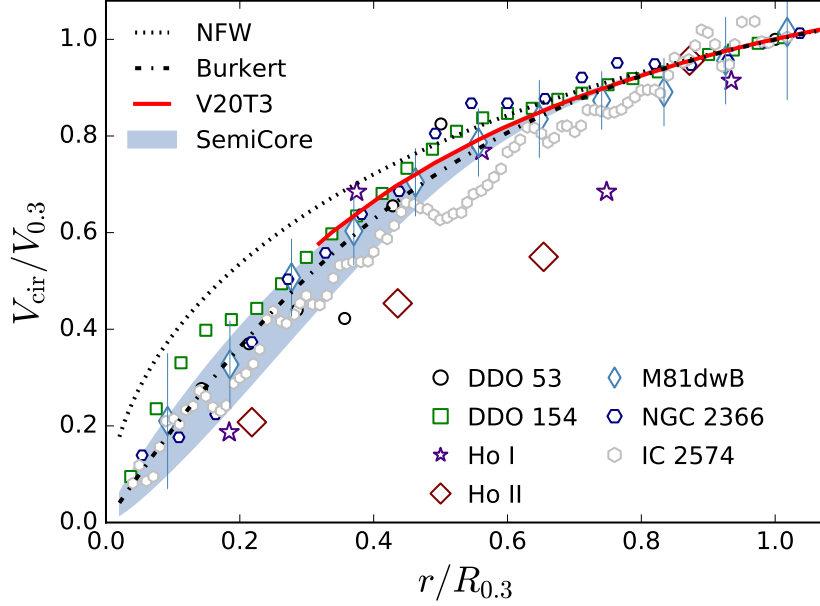


Figure 3.8: Scaled rotation curves of the DDM halo V20T3 and 7 dwarf galaxies taken from THINGS [93]. The theoretical curves based on NFW and Burkert profiles are also plotted as black dotted line and dot-dashed line, respectively. The red solid line shows the curve of V20T3 for $r \geq r_{\text{rel}}$, where statistical uncertainties are negligible. The systematic uncertainty for $V_{\text{cir}}/V_{0.3}$ at r_{rel} is estimated to be about 3%. For larger radii, the systematic uncertainties become unimportant. We also have 2% uncertainty in the value of $R_{0.3}$, the effect of which on $V_{\text{cir}}/V_{0.3}$ can also be safely neglected. For the observational data, baryons have been subtracted. The light blue region is the prediction of the *SemiCore* model with the same set of decay parameters as V20T3. Error bars for the galaxy M81dwB are attached to show the typical uncertainty in observation.

though a bit steeper, the scaled DDM rotation curve from N-body simulation is indistinguishable from that of the Burkert profile within the uncertainties of observation. Our N-body results confirm that the *core-cusp* problem can be solved in the DDM model with a recoiling velocity V_k smaller than the typical escape velocities of dwarf halos [85], provided that the decay half-life $\tau^* \lesssim 7.0$ Gyr.

In Figure 3.9, we show the positions of the 9 zoom-in dwarf halos in the DDM parameter space. They reside inside a region, shown in gold, where dark matter decays have prominent effects on the number density and inner structure of dwarf galaxies [41]. The 5 zoom-in halos with a much more flattened central density are indicated by red dots while the remaining 4 by blue dots. For $V_k = 20.0$ km/s and $\tau^* = 6.93$ Gyr, Wang et al.(2014) [42] have run a zoom-in simulation on a Milky-Way sized host halo with the PMK10 algorithm. They found that the circular velocity profiles of the 15 most massive subhalos pass through most of the data points from the 9 classical Milky-Way dSphs, and therefore the *too-big-to-fail* problem is potentially resolved. The brown strip is the parameter region, shown by Abdelqader and

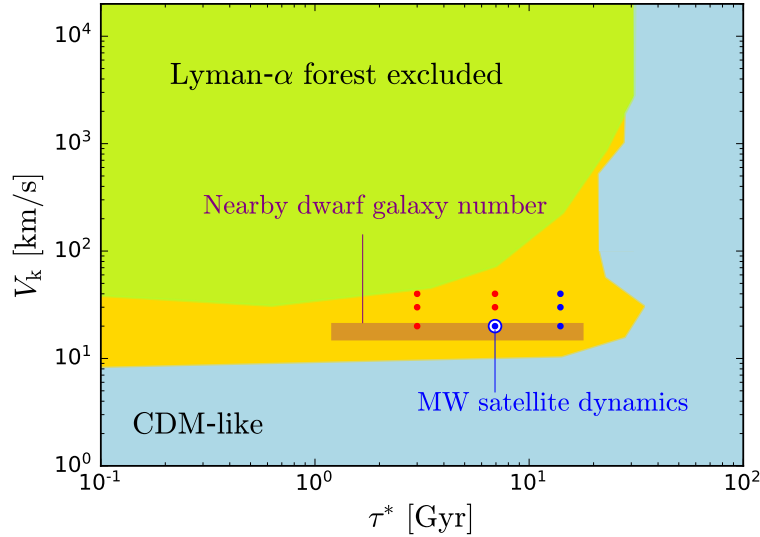


Figure 3.9: Constrained DDM parameter space. The green-yellow region is ruled out by the Lyman- α forest data [39]. The DDM model in the light-blue region behaves like the CDM model in describing the cosmic structure formation. The gold region is outlined by Peter and Benson (2010) [41] and is interesting for small-scale problems of CDM. The blue and red points mark the 9 level-12 zoom-in dwarf halos in this work, with the blue and red color indicating cuspy and cored halo density profile respectively. For the blue point $V_k = 20.0$ km/s and $\tau^* = 6.93$ Gyr, the dynamics of Milky-Way satellite galaxies in the DDM model is explored in Wang et al. (2013). [39]. The brown strip is given by Abdelqader and Melia (2008) [40] where the deficit of dwarf galaxies in our local group can be accounted for in the DDM model.

Melia [40] using a semi-analytic model that incorporates dark matter decays in the hierarchical formation history of dark matter halos, that can account for the deficit of dwarf galaxies in our local group, a puzzle closely related to the *missing-satellites* problem [19, 20]. It can be seen that several different CDM

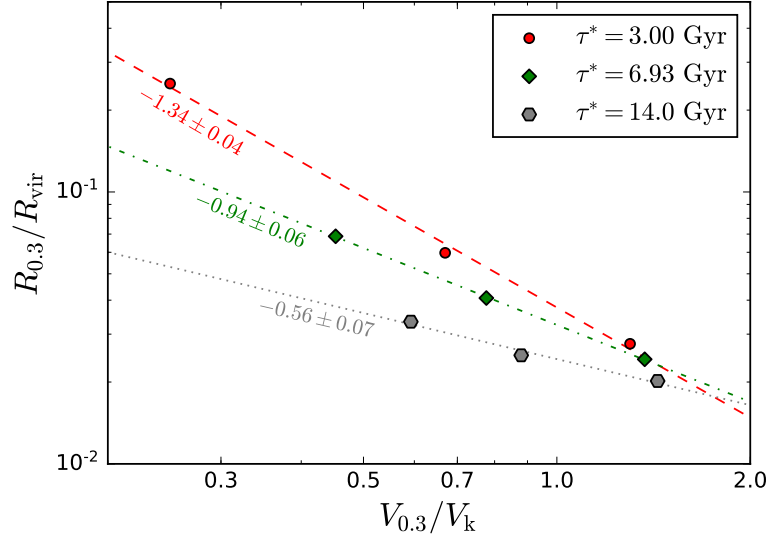


Figure 3.10: Relation between $R_{0.3}$ and $V_{0.3}$ for DDM zoom-in dwarf halos with the same half-life τ^* . The red circles, green diamonds and gray hexagons refer to halos with $\tau^* = 3.00$, 6.93 , and 14.0 Gyr, respectively. There is 2% uncertainty in $R_{0.3}$ and 0.6% uncertainty in $V_{0.3}$. The best-fit power law curves for data points with $\tau^* = 3.00$, 6.93 , and 14.0 Gyr are shown with red dashed, green dot-dashed and dotted line respectively. The best-fit power indexes are also shown near each line for reference.

problems can be solved by a common parameter subspace in the DDM model.

In Figure 3.10, we show that $R_{0.3}$ and $V_{0.3}$ have a power-law relation for DDM zoom-in dwarf halos:

$$\frac{R_{0.3}}{R_{\text{vir}}} \propto \left(\frac{V_{0.3}}{V_k} \right)^{-\beta(\tau^*)}, \quad (3.23)$$

where the power index β increases as τ^* decreases. Given the values of $R_{0.3}/R_{\text{vir}}$ and $V_{0.3}$, both being observable quantities, a re-

lation between V_k and τ^* can be derived from relation (3.23). As V_k and τ^* are constants in the DDM model, from relation (3.23) we also find

$$\frac{V_{0.3}}{V_{\text{vir}}} \propto \left(\frac{R_{0.3}}{R_{\text{vir}}} \right)^{-1/\beta} M_{\text{vir}}^{-1/3}. \quad (3.24)$$

Since dwarf halos have a narrow virial mass spectrum and Equation (3.24) depends only weakly on M_{vir} , an approximate universal density profile is expected. The observed value of β can then be used to measure τ^* . We will study this possibility in a future work.

□ End of chapter.

Chapter 4

Conclusion

We have improved the DDM N-body algorithm by combining the advantages of the PMK10 and CCT15 algorithms. The new algorithm outperforms PMK10 in accuracy while demanding much less computing resources than CCT15. Same as CCT15, the new algorithm samples dark matter decays only at certain times and evolves the whole N-body system in a collisionless way at other times. This feature enables the algorithm to be implemented in a plugin module called DDMPLUGIN, which can be used with any CDM N-body code.

We carried out high-resolution cosmological N-body simulations to study the density profiles of dwarf halos with the new DDM algorithm. Good numerical convergence was achieved,

and we succeeded in resolving the halo structure robustly down to 700 pc. Compared to CDM ones, DDM dwarf halos have lower mass concentration and shallower density profile at the inner region. Adopting the orbit-superposition method for mass profile construction, we calculated the DDM halo mass profile by building a simplified semi-analytic model, which features elliptical orbits for daughter particles and incorporates effects of dark matter decays and adiabatic expansion. Although simple, the model predicts DDM halo mass profiles that agree semi-quantitatively with resolved simulation profiles. It therefore illustrates clearly the physics mechanisms involved in the transformation from cusp to core density profiles.

We also calculated the scaled rotation curves for DDM simulation halos and compared them with 7 dwarf galaxies from THINGS. The shape of the DDM rotation curve is shallower than that based on the NFW profile but steeper than the Burkert's. For the three halos with $\tau^* = 3.0$ Gyr and the two halos with $\tau^* = 6.93$ Gyr and $V_k > 20.0$ km/s, their scaled rotation curves are indistinguishable from that of the Burkert profile within the uncertainties of observation. This shows that the

DDM model can resolve the *core-cusp* problem inside a quite large parameter subspace. Furthermore, we show that there is an approximate universal power-law relation between $V_{0.3}/V_{\text{vir}}$ and $R_{0.3}/R_{\text{vir}}$ for dwarf halos, which can help to extract DDM parameters from observation data. Together with previous studies, this work supports the DDM cosmology, which keeps the success of CDM at large scale and reconciles the differences between observations and predictions from N-body simulations at small scale.

□ End of chapter.

Appendix A

Angular momentum profile in stellar mass

To obtain the $j_{\text{mod}}(r, \theta) - M_{\star}$ relation, one needs to relate the halo mass M_{vir} to a stellar mass M_{\star} . This can be done by using the following stellar mass - halo mass relation [59],

$$\log_{10}(M_{\star}) = \log_{10}(\epsilon M_1) + f \left[\log_{10} \left(\frac{M_{\text{vir}}}{M_1} \right) \right] - f(0), \quad (\text{A.1})$$

with

$$f(x) = -\log_{10}(10^{\alpha x} + 1) + \delta \frac{[\log_{10}(1 + \exp(x))]^{\gamma}}{1 + \exp(10^{-x})}, \quad (\text{A.2})$$

where masses are in the solar mass M_{\odot} . There are five parameters in total: M_1 , ϵ , α , δ , and γ . Their values used in our

Table A.1: Model parameters for the specific angular momentum profile

A_{vir}	B_{vir}	E_{vir}	F_{vir}	$\log_{10}(M_1/M_\odot)$	$\log_{10} \epsilon$	α	δ	γ
3.63	0.660	0.95	0.040	11.39	-1.685	-1.740	4.335	0.531

calculation are listed in Table A.1. For a given M_\star , we use Equation (A.1) to derive its corresponding M_{vir} and then apply our model to calculate the dark matter halo's specific angular momentum profile:

$$j_{\text{mod}}(r, \theta) = j_s \frac{(r/r_s)^2}{(1 + r/r_s)^4} \sin^2(\theta/\theta_s), \quad (\text{A.3})$$

with

$$\frac{j_s}{h^{-1} \text{ Mpc km s}^{-1}} = A_{\text{vir}} \left(\frac{M_{\text{vir}}}{10^{10} h^{-1} M_\odot} \right)^{B_{\text{vir}}}, \quad (\text{A.4})$$

$$r_s = E_{\text{vir}} \left(\frac{M_{\text{vir}}}{10^{10} h^{-1} M_\odot} \right)^{F_{\text{vir}}}, \quad (\text{A.5})$$

and

$$\theta_s = 1.096. \quad (\text{A.6})$$

Values for parameters A_{vir} , B_{vir} , E_{vir} , and F_{vir} are also summarized in Table A.1.

□ **End of chapter.**

Appendix B

Documentation for the code: DDMPLUGIN

B.1 Auxiliary daughter and permanent daughter

In our algorithm, the mother particles decay and give birth to daughter particles only at a limited number of decaying instances, called breakpoints. When a breakpoint arrives, each mother particle is splitted into a less-massive mother particle and a daughter particle at the mother particle's position. The newly generated daughter particles are called auxiliary daughters. The mass-splitting procedure increases the total number of simulation particles by N , which is the number of mother

particles. To save memory as well as to speed up the whole simulation¹, the code only tracks the motion of these N auxiliary daughters for one phase. A phase is the time interval between two adjacent breakpoints. When the simulation arrives at the next breakpoint, the auxiliary daughters born at last breakpoint will undergo a selection process such that only a fraction of them survive and are renamed as permanent daughters. This fraction is called the survival rate η of auxiliary daughters. Other auxiliary daughter particles are eliminated so that the memory occupied by them is released. For permanent daughters, once flagged, their trajectories will be traced to the end of the simulation. Therefore there are two states of a daughter particle appearing in a simulation: auxiliary and permanent.

The role of the auxiliary daughters is to help conserve the local matter mass when decay occurs, a basic conservation observed in previous DDM codes [71, 70]. After diffusing into the local environment, these auxiliary daughters are replaced by permanent daughters, which have a smaller population, hence heavier. The transition from auxiliary state to permanent state decreases the resolution of daughter particles. Numerical side-

effect shall be introduced from the resolution degradation. However, it can be controlled and studied by tuning η , the survival rate of auxiliary daughters. Suppose there are N mother particles and they will go through N_s breakpoints during the whole simulation, and the simulation will contain $N_f N$ permanent daughters when it is finished, then the survival rate is

$$\eta = N_f / N_s. \quad (\text{B.1})$$

N_f is also an integer and we require that $N_f \leq N_s$.

B.2 Auxiliary-permanent transition

The auxiliary-permanent transition is implemented as follows in the DDMPLUGIN code. First, the particle ID I_{aux} of an auxiliary daughter is decomposed into a pair of integers (q, p) :

$$I_{aux} = qN_s + p. \quad (\text{B.2})$$

Auxiliary daughters satisfying $p < N_f$ survive and are flagged as permanent daughters. Auxiliary daughters with $p \geq N_f$ are eliminated from the simulation. Once an auxiliary daughter is

flagged to be permanent, its mass and ID have to be modified while its position and velocity are retained. The particle mass needs modification such that the daughter particles' total mass is unaffected by the transtion:

$$m_{pmt} = m_{aux} \frac{N_s}{N_f}, \quad (\text{B.3})$$

where m_{pmt} and m_{aux} are the particle masses of permanent and auxiliary daughters, respectively. A new ID I_{pmt} is assigned to the permanent daughter in order to distinguish it from its pre-transition auxiliary state:

$$I_{pmt} = N_{tot} + I_{ini} + (q - q_{min})N_f + (p - p_{min}), \quad (\text{B.4})$$

where N_{tot} is the total number of particles in the simulation just before the transition, I_{ini} is the smallest ID taken by the simulation², (q_{min}, p_{min}) is the integer pair derived from the minimum ID of the auxiliary daughters that are flagged to be permanent daughters. The ID assignment scheme (B.4) ensures that particle ID in the simulation is continuous and there is no spatial bias in the selection process. Position and velocity are invariant

under the auxiliary-permanent transition:

$$\boldsymbol{x}_{pmt} = \boldsymbol{x}_{aux}, \quad (\text{B.5})$$

$$\boldsymbol{v}_{pmt} = \boldsymbol{v}_{aux}. \quad (\text{B.6})$$

The auxiliary-permanent transition will also be applied to output particle data.

B.3 Decay of mother particles

At each breakpoint, mother particles will decay and release auxiliary daughter particles. Due to the random nature of dark matter decay, the N-body mother particles do not receive velocity kicks when decay occurs. Only their masses are affected and reduced by m_{aux} , the mass of a auxiliary particle:

$$m'_{mom} = m_{mom} - m_{aux}, \quad (\text{B.7})$$

where m_{mom} and m'_{mom} are the masses of a mother particle just before and after the decay. Other information associated with the post-decay mother is exactly the same as that of the pre-decay mother. As for the newly generated auxiliary daughter

particles, the decay kicks them away from their mother particles:

$$\mathbf{x}_{aux} = \mathbf{x}_{mom}, \quad (\text{B.8})$$

$$\mathbf{v}_{aux} = \mathbf{v}_{mom} + V_k \mathbf{n}, \quad (\text{B.9})$$

where V_k is the recoil velocity, \mathbf{n} is a unit vector pointing to a random direction. The IDs of the auxiliary daughters are assigned as follows:

$$I_{aux} = N_{tot,ini} + I_{ini} + I_{off}, \quad (\text{B.10})$$

where $N_{tot,ini}$ is the total number of particles in the initial condition, I_{ini} is the smallest ID taken by the simulation, and I_{off} is an integer ranging from 0 to $N - 1$. Each auxiliary daughter particle gets a different value of I_{off} randomly hence their IDs are different from each other. Mass of auxiliary daughter particles are determined by mother particle's half-time τ and the number of breakpoints N_s :

$$m_{aux} = m_{mom,ini} \frac{1 - \exp(-\ln 2 T_{sys}/\tau)}{N_s}, \quad (\text{B.11})$$

where $m_{mom,ini}$ is the initial mass of a mother particle, and T_{sys} is the age of the system when the simulation ends. For cosmological N-body simulations, T_{sys} is just the age of our universe, which exact value depends on cosmological parameters.

In the DDMPLUGIN code, mother particles, auxiliary daughter particles and permanent daughter particles are all labelled as halo particles, which is type 1 according to Gadget’s classification. It is possible to assign auxiliary daughters and permanent daughters to different types. However, it will slow down the whole simulation.

□ **End of chapter.**

¹GADGET-2 and GADGET-3 applies TreePM algorithm for gravitational force evaluation, which is faster than a pure Tree code and slower than a pure PM code. The force calculation time scales as $N_p \ln N_p$ for Tree code and scales as N_p for a PM code, where N_p is the total number of simulation particles [94].

²The smallest Id can vary for different initial condition generators. For initial conditions generated by *MUSIC*, the smallest Id is 0. While for *2LPT*, Id starts from 1.

Appendix C

Numerical tests

C.1 Transfer function

Here we test the effects of uncertainties in the transfer function on the dark matter halo’s average density profile $\bar{\rho}(r)$. Two different transfer functions, the default BBKS and Eisenstein-Hu [95] with baryonic features, are used in the test. We run level-11 resolution CDM zoom-in simulations and measure the resulting profiles at $z = 0$. The results are shown in the left panel of Figure C.1. The uncertainties on the average density profile are well within 4% for most resolved radii. Hence the choice of transfer functions has little impact on our results.

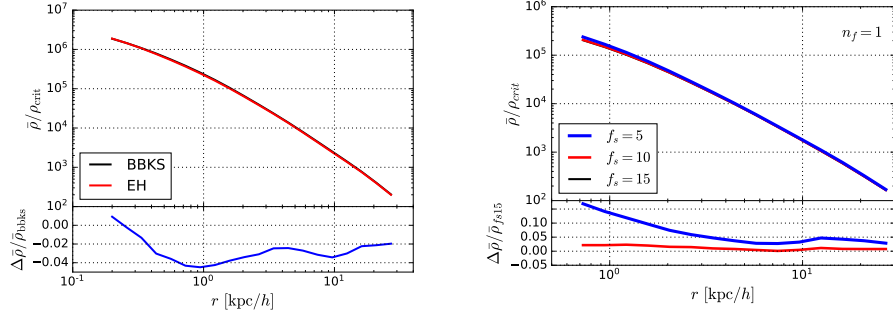


Figure C.1: Left panel: Effects of transfer function variation on dark matter halo average density profile $\bar{\rho}(r)$. Densities are normalized by the current critical density ρ_{crit} . The black solid lines are for the BBKS transfer function while red solid lines are for the Eisenstein-Hu transfer function, and the blue lines show the relative differences between them normalized by BBKS's results. The average density profile is not affected by the two-body relaxation for radii larger than 0.6 kpc/h. Right panel: Effects of the numerical parameter f_s on $\bar{\rho}(r)$. DDM simulations for this test all use $V_k = 20.0$ km/s, $\tau^* = 3.0$ Gyr and $n_f = 1$. All profiles are measured at redshift 0 and plotted down to the inner-most resolved radii. The blue, red and black solid lines represent profiles for $f_s = 5, 10, 15$ respectively. The profiles with $f_s = 15$ serve as the baselines for comparison.

C.2 f_s

We used three values to test the effects of f_s on the halo average density profile $\bar{\rho}(r)$: $f_s = 5, 10$ and 15 with n_f being 1. The decayed mass fraction per phase are 19.2%, 9.59% and 6.39% for $f_s = 5, 10$ and 15 , respectively. From the right panel of Figure C.1, it can be seen that the average densities near a halo's center are more easily affected by varying f_s . It is clear that convergence can be achieved by increasing the value of f_s .

The relative differences in the average density profiles between $f_s = 10$ and $f_s = 15$ are within 3%.

Bibliography

- [1] E. L. Wright, S. S. Meyer, C. L. Bennett, N. W. Boggess, E. S. Cheng, M. G. Hauser, A. Kogut, C. Lineweaver, J. C. Mather, G. F. Smoot, R. Weiss, S. Gulkis, G. Hinshaw, M. Janssen, T. Kelsall, P. M. Lubin, Jr. Moseley, S. H., T. L. Murdock, R. A. Shafer, R. F. Silverberg, and D. T. Wilkinson. Interpretation of the Cosmic Microwave Background Radiation Anisotropy Detected by the COBE Differential Microwave Radiometer. *ApJ*, 396:L13, Sep 1992.
- [2] D. N. Spergel, L. Verde, H. V. Peiris, E. Komatsu, M. R.olta, C. L. Bennett, M. Halpern, G. Hinshaw, N. Jarosik, A. Kogut, M. Limon, S. S. Meyer, L. Page, G. S. Tucker, J. L. Weiland, E. Wollack, and E. L. Wright. First-Year Wilkinson Microwave Anisotropy Probe (WMAP) Observations: Determination of Cosmological Parameters. *ApJS*,

- 148(1):175–194, Sep 2003.
- [3] Volker Springel, Carlos S. Frenk, and Simon D. M. White. The large-scale structure of the Universe. *Nature*, 440(7088):1137–1144, Apr 2006.
- [4] F. Zwicky. Die Rotverschiebung von extragalaktischen Nebeln. *Helv. Phys. Acta*, 6:110–127, 1933. [Gen. Rel. Grav.41,207(2009)].
- [5] A. Bosma. 21-cm line studies of spiral galaxies. II. The distribution and kinematics of neutral hydrogen in spiral galaxies of various morphological types. *AJ*, 86:1825–1846, Dec 1981.
- [6] M. Markevitch, A. H. Gonzalez, L. David, A. Vikhlinin, S. Murray, W. Forman, C. Jones, and W. Tucker. A Text-book Example of a Bow Shock in the Merging Galaxy Cluster 1E 0657-56. *ApJ*, 567(1):L27–L31, Mar 2002.
- [7] Planck Collaboration, Y. Akrami, F. Arroja, M. Ashdown, J. Aumont, C. Baccigalupi, M. Ballardini, A. J. Banday, R. B. Barreiro, N. Bartolo, S. Basak, R. Battye, K. Benabed, J. P. Bernard, M. Bersanelli, P. Bielewicz, J. J.

Bock, J. R. Bond, J. Borrill, F. R. Bouchet, F. Boulanger, M. Bucher, C. Burigana, R. C. Butler, E. Calabrese, J. F. Cardoso, J. Carron, B. Casaponsa, A. Challinor, H. C. Chiang, L. P. L. Colombo, C. Combet, D. Contreras, B. P. Crill, F. Cuttaia, P. de Bernardis, G. de Zotti, J. Delabrouille, J. M. Delouis, F. X. Désert, E. Di Valentino, C. Dickinson, J. M. Diego, S. Donzelli, O. Doré, M. Douspis, A. Ducout, X. Dupac, G. Efstathiou, F. Elsner, T. A. Enßlin, H. K. Eriksen, E. Falgarone, Y. Fantaye, J. Fergusson, R. Fernandez-Cobos, F. Finelli, F. Forastieri, M. Frailis, E. Franceschi, A. Frolov, S. Galeotta, S. Galli, K. Ganga, R. T. Génova-Santos, M. Gerbino, T. Ghosh, J. González-Nuevo, K. M. Górski, S. Gratton, A. Gruppuso, J. E. Gudmundsson, J. Hamann, W. Handley, F. K. Hansen, G. Helou, D. Herranz, E. Hivon, Z. Huang, A. H. Jaffe, W. C. Jones, A. Karakci, E. Keihänen, R. Keskitalo, K. Kiiveri, J. Kim, T. S. Kisner, L. Knox, N. Krachmalnicoff, M. Kunz, H. Kurki-Suonio, G. Lagache, J. M. Lamarre, M. Langer, A. Lasenby, M. Lattanzi, C. R. Lawrence, M. Le Jeune, J. P. Leahy, J. Lesgourgues,

F. Levrier, A. Lewis, M. Liguori, P. B. Lilje, M. Lilley, V. Lindholm, M. López-Caniego, P. M. Lubin, Y. Z. Ma, J. F. Macías-Pérez, G. Maggio, D. Maino, N. Mandolesi, A. Mangilli, A. Marcos-Caballero, M. Maris, P. G. Martin, E. Martínez-González, S. Matarrese, N. Mauri, J. D. McEwen, P. D. Meerburg, P. R. Meinhold, A. Melchiorri, A. Mennella, M. Migliaccio, M. Millea, S. Mitra, M. A. Miville-Deschênes, D. Molinari, A. Moneti, L. Montier, G. Morgante, A. Moss, S. Mottet, M. Münchmeyer, P. Natoli, H. U. Nørgaard-Nielsen, C. A. Oxborrow, L. Pagano, D. Paoletti, B. Partridge, G. Patanchon, T. J. Pearson, M. Peel, H. V. Peiris, F. Perrotta, V. Pettorino, F. Piacentini, L. Polastri, G. Polenta, J. L. Puget, J. P. Rachen, M. Reinecke, M. Remazeilles, A. Renzi, G. Rocha, C. Rosset, G. Roudier, J. A. Rubiño-Martín, B. Ruiz-Granados, L. Salvati, M. Sandri, M. Savelainen, D. Scott, E. P. S. Shellard, M. Shiraishi, C. Sirignano, G. Sirri, L. D. Spencer, R. Sunyaev, A. S. Suur-Uski, J. A. Tauber, D. Tavagnacco, M. Tenti, L. Terenzi, L. Toffolatti, M. Tomasi, T. Trombetti, J. Valiviita, B. Van Tent, L. Vibert, P. Vielva,

- F. Villa, N. Vittorio, B. D. Wandelt, I. K. Wehus, M. White, S. D. M. White, A. Zacchei, and A. Zonca. Planck 2018 results. I. Overview and the cosmological legacy of Planck. *arXiv e-prints*, page arXiv:1807.06205, Jul 2018.
- [8] S. D. M. White, C. S. Frenk, and M. Davis. Clustering in a neutrino-dominated universe. *ApJ*, 274:L1–L5, Nov 1983.
- [9] P. J. E. Peebles. Large-scale background temperature and mass fluctuations due to scale-invariant primeval perturbations. *ApJ*, 263:L1–L5, Dec 1982.
- [10] G. R. Blumenthal, S. M. Faber, J. R. Primack, and M. J. Rees. Formation of galaxies and large-scale structure with cold dark matter. *Nature*, 311:517–525, Oct 1984.
- [11] C. S. Frenk, S. D. M. White, G. Efstathiou, and M. Davis. Cold dark matter, the structure of galactic haloes and the origin of the Hubble sequence. *Nature*, 317(6038):595–597, Oct 1985.
- [12] M. Davis, G. Efstathiou, C. S. Frenk, and S. D. M. White. The evolution of large-scale structure in a universe dominated by cold dark matter. *ApJ*, 292:371–394, May 1985.

- [13] John Dubinski and R. G. Carlberg. The Structure of Cold Dark Matter Halos. *ApJ*, 378:496, Sep 1991.
- [14] J. F. Navarro, C. S. Frenk, and S. D. M. White. The Structure of Cold Dark Matter Halos. *ApJ*, 462:563, May 1996.
- [15] Ricardo A. Flores and Joel R. Primack. Observational and Theoretical Constraints on Singular Dark Matter Halos. *ApJ*, 427:L1, May 1994.
- [16] Ben Moore. Evidence against dissipation-less dark matter from observations of galaxy haloes. *Nature*, 370(6491):629–631, Aug 1994.
- [17] B. Moore, T. Quinn, F. Governato, J. Stadel, and G. Lake. Cold collapse and the core catastrophe. *MNRAS*, 310(4):1147–1152, Dec 1999.
- [18] W. J. G. de Blok. The Core-Cusp Problem. *Advances in Astronomy*, 2010:789293, Jan 2010.
- [19] Anatoly Klypin, Andrey V. Kravtsov, Octavio Valenzuela, and Francisco Prada. Where Are the Missing Galactic Satellites? *ApJ*, 522(1):82–92, Sep 1999.

- [20] B. Moore, S. Ghigna, F. Governato, G. Lake, T. Quinn, J. Stadel, and P. Tozzi. Dark Matter Substructure within Galactic Halos. *ApJ*, 524:L19–L22, October 1999.
- [21] Mario L. Mateo. Dwarf Galaxies of the Local Group. *ARA&A*, 36:435–506, Jan 1998.
- [22] Michael Boylan-Kolchin, James S. Bullock, and Manoj Kaplinghat. Too big to fail? The puzzling darkness of massive Milky Way subhaloes. *MNRAS*, 415(1):L40–L44, Jul 2011.
- [23] James S. Bullock and Michael Boylan-Kolchin. Small-Scale Challenges to the Λ CDM Paradigm. *ARA&A*, 55(1):343–387, Aug 2017.
- [24] Julio F. Navarro, Vincent R. Eke, and Carlos S. Frenk. The cores of dwarf galaxy haloes. *MNRAS*, 283(3):L72–L78, Dec 1996.
- [25] Andrew Pontzen and Fabio Governato. How supernova feedback turns dark matter cusps into cores. *MNRAS*, 421(4):3464–3471, Apr 2012.

- [26] Alejandro Benítez-Llambay, Carlos S. Frenk, Aaron D. Ludlow, and Julio F. Navarro. Baryon-induced dark matter cores in the EAGLE simulations. *MNRAS*, 488(2):2387–2404, Sep 2019.
- [27] Aaron A. Dutton, Andrea V. Macciò, Tobias Buck, Keri L. Dixon, Marvin Blank, and Aura Obreja. NIHAO XX: the impact of the star formation threshold on the cusp-core transformation of cold dark matter haloes. *MNRAS*, 486(1):655–671, Jun 2019.
- [28] F. Governato, C. Brook, L. Mayer, A. Brooks, G. Rhee, J. Wadsley, P. Jonsson, B. Willman, G. Stinson, T. Quinn, and P. Madau. Bulgeless dwarf galaxies and dark matter cores from supernova-driven outflows. *Nature*, 463(7278):203–206, Jan 2010.
- [29] Edouard Tollet, Andrea V. Macciò, Aaron A. Dutton, Greg S. Stinson, Liang Wang, Camilla Penzo, Thales A. Gutcke, Tobias Buck, Xi Kang, Chris Brook, Arianna Di Cintio, Ben W. Keller, and James Wadsley. NIHAO - IV: core creation and destruction in dark matter density pro-

- files across cosmic time. *MNRAS*, 456(4):3542–3552, Mar 2016.
- [30] T. K. Chan, D. Kereš, J. Oñorbe, P. F. Hopkins, A. L. Muratov, C. A. Faucher-Giguère, and E. Quataert. The impact of baryonic physics on the structure of dark matter haloes: the view from the FIRE cosmological simulations. *MNRAS*, 454(3):2981–3001, Dec 2015.
- [31] Till Sawala, Carlos S. Frenk, Azadeh Fattahi, Julio F. Navarro, Richard G. Bower, Robert A. Crain, Claudio Dalla Vecchia, Michelle Furlong, John. C. Helly, Adrian Jenkins, Kyle A. Oman, Matthieu Schaller, Joop Schaye, Tom Theuns, James Trayford, and Simon D. M. White. The APOSTLE simulations: solutions to the Local Group’s cosmic puzzles. *MNRAS*, 457(2):1931–1943, Apr 2016.
- [32] Andrey V. Kravtsov, Anatoly A. Klypin, James S. Bullock, and Joel R. Primack. The Cores of Dark Matter-dominated Galaxies: Theory versus Observations. *ApJ*, 502(1):48–58, Jul 1998.

- [33] P. Salucci and A. Burkert. Dark Matter Scaling Relations. *ApJ*, 537(1):L9–L12, Jul 2000.
- [34] A. Burkert. The Structure of Dark Matter Halos in Dwarf Galaxies. *ApJ*, 447:L25–L28, Jul 1995.
- [35] Julio F. Navarro. Dwarf Galaxies as Cosmological Probes. In Kristen B. W. McQuinn and Sabrina Stierwalt, editors, *Dwarf Galaxies: From the Deep Universe to the Present*, volume 344 of *IAU Symposium*, pages 455–463, Oct 2019.
- [36] Manoj Kaplinghat. Dark matter from early decays. *Phys. Rev. D*, 72(6):063510, Sep 2005.
- [37] Louis E. Strigari, Manoj Kaplinghat, and James S. Bullock. Dark matter halos with cores from hierarchical structure formation. *Phys. Rev. D*, 75(6):061303, Mar 2007.
- [38] Kyriakos Vattis, Savvas M. Koushiappas, and Abraham Loeb. Dark matter decaying in the late Universe can relieve the H_0 tension. *Phys. Rev. D*, 99(12):121302, Jun 2019.
- [39] Mei-Yu Wang, Rupert A. C. Croft, Annika H. G. Peter, Andrew R. Zentner, and Chris W. Purcell. Lyman- α for-

- est constraints on decaying dark matter. *Phys. Rev. D*, 88(12):123515, Dec 2013.
- [40] Majd Abdelqader and Fulvio Melia. Decaying dark matter and the deficit of dwarf haloes. *MNRAS*, 388(4):1869–1878, Aug 2008.
- [41] Annika H. G. Peter and Andrew J. Benson. Dark-matter decays and milky way satellite galaxies. *Phys. Rev. D*, 82:123521, Dec 2010.
- [42] Mei-Yu Wang, Annika H. G. Peter, Louis E. Strigari, Andrew R. Zentner, Bryan Arant, Shea Garrison-Kimmel, and Miguel Rocha. Cosmological simulations of decaying dark matter: implications for small-scale structure of dark matter haloes. *MNRAS*, 445(1):614–629, Nov 2014.
- [43] James Binney and Scott Tremaine. *Galactic Dynamics: Second Edition*. 2008.
- [44] Alan P. Lightman and Stuart L. Shapiro. The dynamical evolution of globular clusters. *Reviews of Modern Physics*, 50(2):437–481, Apr 1978.

- [45] S. von Hoerner. Die numerische Integration des n-Körper-Problems für Sternhaufen. I. ZAp, 50:184–214, Jan 1960.
- [46] S. von Hoerner. Die numerische Integration des n-Körper-Problems für Sternhaufen, II. ZAp, 57:47–82, Jan 1963.
- [47] S. J. Aarseth. Dynamical evolution of clusters of galaxies, I. MNRAS, 126:223, Jan 1963.
- [48] R. W. Hockney and J. W. Eastwood. *Computer simulation using particles*. 1988.
- [49] Josh Barnes and Piet Hut. A hierarchical $O(N \log N)$ force-calculation algorithm. Nature, 324(6096):446–449, Dec 1986.
- [50] Edmund Bertschinger. Simulations of Structure Formation in the Universe. ARA&A, 36:599–654, Jan 1998.
- [51] J. Barnes and G. Efstathiou. Angular momentum from tidal torques. ApJ, 319:575–600, August 1987.
- [52] Philip Bett, Vincent Eke, Carlos S. Frenk, Adrian Jenkins, and Takashi Okamoto. The angular momentum of cold dark

- matter haloes with and without baryons. *Monthly Notices of the Royal Astronomical Society*, 404(3):1137–1156, 05 2010.
- [53] J. S. Bullock, A. Dekel, T. S. Kolatt, A. V. Kravtsov, A. A. Klypin, C. Porciani, and J. R. Primack. A Universal Angular Momentum Profile for Galactic Halos. *ApJ*, 555:240–257, July 2001.
- [54] Anatoly A. Klypin, Sebastian Trujillo-Gomez, and Joel Primack. DARK MATTER HALOS IN THE STANDARD COSMOLOGICAL MODEL: RESULTS FROM THE BOLSHOI SIMULATION. *The Astrophysical Journal*, 740(2):102, oct 2011.
- [55] Shihong Liao, Jianxiong Chen, and M. C. Chu. A Universal Angular Momentum Profile for Dark Matter Halos. *ApJ*, 844(1):86, Jul 2017.
- [56] Shihong Liao, Dalong Cheng, M. C. Chu, and Jiayu Tang. Angular Momentum-Mass Relation for Dark Matter Halos. *ApJ*, 809(1):64, Aug 2015.
- [57] P. S. Behroozi, R. H. Wechsler, and C. Conroy. The Average Star Formation Histories of Galaxies in Dark Matter Halos

from $z = 0-8$. *ApJ*, 770:57, June 2013.

- [58] Benjamin P. Moster, Thorsten Naab, and Simon D. M. White. Galactic star formation and accretion histories from matching galaxies to dark matter haloes . *Monthly Notices of the Royal Astronomical Society*, 428(4):3121–3138, 12 2012.
- [59] A. V. Kravtsov, A. A. Vikhlinin, and A. V. Meshcheryakov. Stellar Mass—Halo Mass Relation and Star Formation Efficiency in High-Mass Halos. *Astronomy Letters*, 44(1):8–34, Jan 2018.
- [60] L. Mestel. On the Galactic Law of Rotation. *Monthly Notices of the Royal Astronomical Society*, 126(6):553–575, 11 1963.
- [61] P. J. E. Peebles. Origin of the Angular Momentum of Galaxies. *ApJ*, 155:393, February 1969.
- [62] S. Michael Fall and George Efstathiou. Formation and rotation of disc galaxies with haloes. *Monthly Notices of the Royal Astronomical Society*, 193(2):189–206, 11 1980.

- [63] H. J. Mo, Shude Mao, and Simon D. M. White. The formation of galactic discs. *Monthly Notices of the Royal Astronomical Society*, 295(2):319–336, 04 1998.
- [64] D. Obreschkow and K. Glazebrook. FUNDAMENTAL MASS-SPIN-MORPHOLOGY RELATION OF SPIRAL GALAXIES. *The Astrophysical Journal*, 784(1):26, feb 2014.
- [65] Kirsty M. Butler, Danail Obreschkow, and Se-Heon Oh. ANGULAR MOMENTUM OF DWARF GALAXIES. *The Astrophysical Journal*, 834(1):L4, dec 2016.
- [66] Aditya Chowdhury and Jayaram N. Chengalur. Angular momentum content in gas-rich dwarf galaxies. *Monthly Notices of the Royal Astronomical Society*, 467(4):3856–3863, 02 2017.
- [67] Frank C. van den Bosch, Andreas Burkert, and Rob A. Swaters. The angular momentum content of dwarf galaxies: new challenges for the theory of galaxy formation. *Monthly Notices of the Royal Astronomical Society*, 326(3):1205–1215, 09 2001.

- [68] James Binney, Ortwin Gerhard, and Joseph Silk. The dark matter problem in disc galaxies. *Monthly Notices of the Royal Astronomical Society*, 321(3):471–474, 03 2001.
- [69] C. B. Brook, F. Governato, R. Rokaer, G. Stinson, A. M. Brooks, J. Wadsley, T. Quinn, B. K. Gibson, O. Snaith, K. Pilkington, E. House, and A. Pontzen. Hierarchical formation of bulgeless galaxies: why outflows have low angular momentum. *Monthly Notices of the Royal Astronomical Society*, 415(2):1051–1060, 07 2011.
- [70] Annika H. G. Peter, Christopher E. Moody, and Marc Kamionkowski. Dark-matter decays and self-gravitating halos. *Phys. Rev. D*, 81(10):103501, May 2010.
- [71] Dalong Cheng, M. C. Chu, and Jiayu Tang. Cosmological structure formation in Decaying Dark Matter models. *Journal of Cosmology and Astro-Particle Physics*, 2015(7):009, Jul 2015.
- [72] Jose Oñorbe, Shea Garrison-Kimmel, Ariyeh H. Maller, James S. Bullock, Miguel Rocha, and Oliver Hahn. How to zoom: bias, contamination and Lagrange volumes in multi-

mass cosmological simulations. *MNRAS*, 437(2):1894–1908, Jan 2014.

[73] Volker Springel. The cosmological simulation code GADGET-2. *MNRAS*, 364(4):1105–1134, Dec 2005.

[74] Planck Collaboration, N. Aghanim, Y. Akrami, M. Ashdown, J. Aumont, C. Baccigalupi, M. Ballardini, A. J. Banday, R. B. Barreiro, N. Bartolo, S. Basak, R. Battye, K. Benabed, J. P. Bernard, M. Bersanelli, P. Bielewicz, J. J. Bock, J. R. Bond, J. Borrill, F. R. Bouchet, F. Boulanger, M. Bucher, C. Burigana, R. C. Butler, E. Calabrese, J. F. Cardoso, J. Carron, A. Challinor, H. C. Chiang, J. Chluba, L. P. L. Colombo, C. Combet, D. Contreras, B. P. Crill, F. Cuttaia, P. de Bernardis, G. de Zotti, J. Delabrouille, J. M. Delouis, E. Di Valentino, J. M. Diego, O. Doré, M. Douspis, A. Ducout, X. Dupac, S. Dusini, G. Efstathiou, F. Elsner, T. A. Enßlin, H. K. Eriksen, Y. Fantaye, M. Farhang, J. Fergusson, R. Fernandez-Cobos, F. Finelli, F. Forastieri, M. Frailis, A. A. Fraisse, E. Franceschi, A. Frolov, S. Galeotta, S. Galli, K. Ganga, R. T. Génova-Santos, M. Gerbino, T. Ghosh, J. González-Nuevo, K. M.

Górski, S. Gratton, A. Gruppuso, J. E. Gudmundsson, J. Hamann, W. Handley, F. K. Hansen, D. Herranz, S. R. Hildebrandt, E. Hivon, Z. Huang, A. H. Jaffe, W. C. Jones, A. Karakci, E. Keihänen, R. Keskitalo, K. Kiveri, J. Kim, T. S. Kisner, L. Knox, N. Krachmalnicoff, M. Kunz, H. Kurki-Suonio, G. Lagache, J. M. Lamarre, A. Lasenby, M. Lattanzi, C. R. Lawrence, M. Le Jeune, P. Lemos, J. Lesgourgues, F. Levrier, A. Lewis, M. Liguori, P. B. Lilje, M. Lilley, V. Lindholm, M. López-Caniego, P. M. Lubin, Y. Z. Ma, J. F. Macías-Pérez, G. Maggio, D. Maino, N. Mandolesi, A. Mangilli, A. Marcos-Caballero, M. Maris, P. G. Martin, M. Martinelli, E. Martínez-González, S. Matarrese, N. Mauri, J. D. McEwen, P. R. Meinhold, A. Melchiorri, A. Mennella, M. Migliaccio, M. Millea, S. Mitra, M. A. Miville-Deschênes, D. Molinari, L. Montier, G. Morgante, A. Moss, P. Natoli, H. U. Nørgaard-Nielsen, L. Pagano, D. Paoletti, B. Partridge, G. Patanchon, H. V. Peiris, F. Perrotta, V. Pettorino, F. Piacentini, L. Polastri, G. Polenta, J. L. Puget, J. P. Rachen, M. Reinecke, M. Remazeilles, A. Renzi, G. Rocha, C. Ros-

- set, G. Roudier, J. A. Rubiño-Martín, B. Ruiz-Granados, L. Salvati, M. Sandri, M. Savelainen, D. Scott, E. P. S. Shellard, C. Sirignano, G. Sirri, L. D. Spencer, R. Sunyaev, A. S. Suur-Uski, J. A. Tauber, D. Tavagnacco, M. Tenti, L. Toffolatti, M. Tomasi, T. Trombetti, L. Valenziano, J. Valiviita, B. Van Tent, L. Vibert, P. Vielva, F. Villa, N. Vittorio, B. D. Wandelt, I. K. Wehus, M. White, S. D. M. White, A. Zacchei, and A. Zonca. Planck 2018 results. VI. Cosmological parameters. *arXiv e-prints*, page arXiv:1807.06209, Jul 2018.
- [75] Oliver Hahn and Tom Abel. Multi-scale initial conditions for cosmological simulations. *MNRAS*, 415(3):2101–2121, Aug 2011.
- [76] J. M. Bardeen, J. R. Bond, N. Kaiser, and A. S. Szalay. The Statistics of Peaks of Gaussian Random Fields. *ApJ*, 304:15, May 1986.
- [77] S. P. D. Gill, A. Knebe, and B. K. Gibson. The evolution of substructure - I. A new identification method. *MNRAS*, 351:399–409, June 2004.

- [78] S. R. Knollmann and A. Knebe. AHF: Amiga’s Halo Finder. *ApJS*, 182:608–624, June 2009.
- [79] Greg L. Bryan and Michael L. Norman. Statistical Properties of X-Ray Clusters: Analytic and Numerical Comparisons. *ApJ*, 495(1):80–99, Mar 1998.
- [80] Toshiyuki Fukushige and Junichiro Makino. Structure of Dark Matter Halos from Hierarchical Clustering. *ApJ*, 557(2):533–545, Aug 2001.
- [81] Benedikt Diemer and Michael Joyce. An accurate physical model for halo concentrations. *arXiv e-prints*, page arXiv:1809.07326, Sep 2018.
- [82] C. Power, J. F. Navarro, A. Jenkins, C. S. Frenk, S. D. M. White, V. Springel, J. Stadel, and T. Quinn. The inner structure of CDM haloes I. A numerical convergence study. *Monthly Notices of the Royal Astronomical Society*, 338(1):14–34, 01 2003.
- [83] Renyue Cen. Decaying Cold Dark Matter Model and Small-Scale Power. *ApJ*, 546(2):L77–L80, Jan 2001.

- [84] Annika H. G. Peter. Mapping the allowed parameter space for decaying dark matter models. *Physical Review D*, 81(8):083511, Apr 2010.
- [85] F. J. Sánchez-Salcedo. Unstable Cold Dark Matter and the Cuspy Halo Problem in Dwarf Galaxies. *ApJ*, 591(2):L107–L110, Jul 2003.
- [86] M. Schwarzschild. A numerical model for a triaxial stellar system in dynamical equilibrium. *ApJ*, 232:236–247, Aug 1979.
- [87] Julio Chanamé. Schwarzschild Models for the Galaxy. *Highlights of Astronomy*, 15:190–191, Nov 2010.
- [88] Bernhard Röttgers, Thorsten Naab, and Ludwig Oser. Stellar orbits in cosmological galaxy simulations: the connection to formation history and line-of-sight kinematics. *Monthly Notices of the Royal Astronomical Society*, 445(2):1065–1083, Dec 2014.
- [89] Oleg Y. Gnedin, Andrey V. Kravtsov, Anatoly A. Klypin, and Daisuke Nagai. Response of Dark Matter Halos to Condensation of Baryons: Cosmological Simulations and

- Improved Adiabatic Contraction Model. *The Astrophysical Journal*, 616(1):16–26, Nov 2004.
- [90] G. R. Blumenthal, S. M. Faber, R. Flores, and J. R. Primack. Contraction of dark matter galactic halos due to baryonic infall. *ApJ*, 301:27–34, February 1986.
- [91] Roland Jesseit, Thorsten Naab, and Andreas Burkert. The Validity of the Adiabatic Contraction Approximation for Dark Matter Halos. *The Astrophysical Journal*, 571(2):L89–L92, Jun 2002.
- [92] Eric Hayashi and Julio F. Navarro. Hiding cusps in cores: kinematics of disc galaxies in triaxial dark matter haloes. *MNRAS*, 373(3):1117–1124, Dec 2006.
- [93] Fabian Walter, Elias Brinks, W. J. G. de Blok, Frank Bigiel, Jr. Kennicutt, Robert C., Michele D. Thornley, and Adam Leroy. THINGS: The H I Nearby Galaxy Survey. *AJ*, 136(6):2563–2647, Dec 2008.
- [94] H. Mo, F. C. van den Bosch, and S. White. *Galaxy Formation and Evolution*. May 2010.

- [95] Daniel J. Eisenstein and Wayne Hu. Baryonic Features in the Matter Transfer Function. *ApJ*, 496(2):605–614, Mar 1998.